

APOBEC3A drives deaminase mutagenesis in human gastric epithelium

Yohan An,^{1,10} Ji-Hyun Lee,^{2,10} Joonoh Lim,^{1,3,10} Jeonghwan Youk,^{1,11} Seongyeol Park,^{1,12} Ji-Hyung Park,^{1,4} Kijong Yi,^{1,3} Taewoo Kim,^{1,13} Chang Hyun Nam,¹ Won Hee Lee,^{1,14} Soo A Oh,³ Yoo Jin Bae,⁵ Thomas M. Klompstra,² Haeun Lee,¹ Jinju Han,¹ Junehwak Lee,⁶ Jung Woo Park,⁶ Jie-Hyun Kim,⁵ Hyunki Kim,⁷ Hugo Snippert,⁸ Bon-Kyoung Koo,^{2,9} and Young Seok Ju^{1,3}

¹Graduate School of Medical Science and Engineering, Korea Advanced Institute of Science and Technology (KAIST), Daejeon 34051, Republic of Korea; ²Center for Genome Engineering, Institute for Basic Science, Yuseong-gu, Daejeon 34126, Republic of Korea; ³Inocras Inc., San Diego, California 92121, USA; ⁴Department of Neurology, Severance Hospital, Yonsei University College of Medicine, Seoul 03722, Republic of Korea; ⁵Department of Internal Medicine, Division of Gastroenterology, Gangnam Severance Hospital, Yonsei University College of Medicine, Gangnam-gu, Seoul 06229, Korea; ⁶Korea Institute of Science and Technology Information, Daejeon 34141, Republic of Korea; ⁷Department of Pathology, Yonsei University College of Medicine, Seoul 03722, Republic of Korea; ⁸Oncode Institute, Center for Molecular Medicine, University Medical Center Utrecht, 3521 AL Utrecht, the Netherlands; ⁹Department of Life Sciences, Pohang University of Science and Technology (POSTECH), Pohang 37673, Republic of Korea

Cancer genomes frequently carry apolipoprotein B mRNA editing catalytic polypeptide-like (APOBEC)-associated DNA mutations, suggesting APOBEC enzymes as innate mutagens during cancer initiation and evolution. However, the pure mutagenic impacts of the specific enzymes among this family remain unclear in human normal cell lineages. Here, we investigate the comparative mutagenic activities of APOBEC3A and APOBEC3B, through whole-genome sequencing of human normal gastric organoid lines carrying doxycycline-inducible APOBEC expression cassettes. Our findings demonstrate that transcriptional upregulation of APOBEC3A leads to the acquisition of a massive number of genomic mutations in just a few cell cycles. In contrast, despite clear deaminase activity and DNA damage, APOBEC3B upregulation does not generate a significant increase in mutations in the gastric epithelium. APOBEC3B-associated mutagenesis remains minimal even in the context of *TP53* inactivation. Further analysis of the mutational landscape following APOBEC3A upregulation reveals a detailed spectrum of APOBEC3A-associated mutations, including indels, primarily 1 bp deletions, clustered mutations, and evidence of selective pressures acting on cells carrying the mutations. Our observations provide a clear foundation for understanding the mutational impact of APOBEC enzymes in human cells.

[Supplemental material is available for this article.]

Large-scale cancer genome studies have revealed various mutational processes in human somatic cells (Alexandrov et al. 2020). APOBEC enzymes, originally known for cytosine deamination in the DNA and RNA against pathogens (Vieira and Soares 2013), were concluded as major endogenous mutagens in cancer (Nik-Zainal et al. 2012a,b; Lawrence et al. 2013; Roberts et al. 2013). About 75% of human cancer types, including bladder transitional cell carcinoma (98%; 381 of 389 samples), breast adenocarcinoma

(83%; 759 of 915 samples), and stomach adenocarcinoma (21%; 101 of 486 samples) showed APOBEC-associated mutational patterns (Sondka et al. 2024). In parallel, the APOBEC-associated mutations are also observed in non-neoplastic normal cells, particularly within the epithelium of the bladder, bronchus, and small intestine (Lawson et al. 2020; Yoshida et al. 2020; Wang et al. 2023). Their mutational spectra, predominantly C>T and C>G base substitutions enriched in TpCpN context (with the mutated cytosine underlined), corresponds to COSMIC signatures SBS2 and SBS13 (<https://cancer.sanger.ac.uk/signatures/>). Of the 11 APOBEC family genes in the human genome, *APOBEC3A* (A3A) and *APOBEC3B* (A3B) have been suggested as major potential contributors to the APOBEC-associated mutations in most human cell types (Roberts et al. 2013; Chan et al. 2015), along with *APOBEC1* in the small intestine (Wang et al. 2023).

The mutagenic potential of A3A and A3B has been investigated across a range of human cancer cell lines (Burns et al. 2013; Petljak et al. 2022; Carpenter et al. 2023). In doing so, APOBEC-

¹⁰These authors contributed equally to this work.

Present addresses: ¹¹Division of Hematology and Medical Oncology, Department of Internal Medicine, Seoul National University College of Medicine and Seoul National University Hospital, Seoul 03080, Republic of Korea; ¹²Stanford Cancer Institute, Stanford University School of Medicine, Stanford, California 94305, USA; ¹³Center for Neurogenetics, Brain and Mind Research Institute, Weill Cornell Medicine, New York, New York 10044, USA; ¹⁴Department of Radiation Oncology, Yonsei Cancer Center, Heavy Ion Therapy Research Institute, Yonsei University College of Medicine, Seoul 03722, Republic of Korea

Corresponding authors: yju@kaist.ac.kr, koobk@ibs.re.kr

Article published online before print. Article, supplemental material, and publication date are at <https://www.genome.org/cgi/doi/10.1101/gr.280338.124>. Freely available online through the *Genome Research* Open Access option.

© 2025 An et al. This article, published in *Genome Research*, is available under a Creative Commons License (Attribution-NonCommercial 4.0 International), as described at <http://creativecommons.org/licenses/by-nc/4.0/>.

associated mutagenic activity has been proposed to occur episodically in cancer cell line models (Petljak et al. 2019). In addition, nonhuman model systems, such as *Mus musculus*, *Saccharomyces cerevisiae*, and the cell line derived from *Gallus gallus domesticus*, have also been utilized for exploring the mutagenic impact of APOBEC enzymes (Chan et al. 2015; Law et al. 2020; DeWeerd et al. 2022; Durfee et al. 2023; Naumann et al. 2023). However, these systems are suboptimal, as these models carry confounding factors, such as additional oncogenic alterations or nonhuman genomic backgrounds. To isolate the pure mutagenic activity of A3A and A3B in human normal cells, we explored genomic alterations in human non-neoplastic gastric organoid lines following APOBEC upregulation, using single-cell cloning and whole-genome sequencing (WGS) (Jager et al. 2019; Pleguezuelos-Manzano et al. 2020; Youk et al. 2024) as well as duplex DNA sequencing (Hoang et al. 2016).

Results

Gastric organoids with doxycycline-inducible APOBEC genes

We established human gastric organoid lines with doxycycline-inducible expression of either A3A or A3B, referred to as hGO_{IA3A} and hGO_{IA3B}, respectively. In these lines, doxycycline treatment simultaneously induces (1) mCherry fluorescence, and (2) expression of the corresponding APOBEC enzyme. To this end, we integrated two cassettes into the genome of gastric organoids (1) expressing rtTA and hygromycin B resistance protein (*CMV-rtTA-Hyg^R*), and (2) expressing APOBEC enzymes and fluorescence protein (*TRE-APOBEC (A3A or A3B)-IRES-mCherry*) using the *piggyBac* transposon system (Fig. 1A; Woodard and Wilson 2015; Wilson et al. 2007). Successfully engineered organoids were selected using hygromycin treatment and subsequently constructed into clonal lines. WGS confirmed their single-cell origin (Supplemental Fig. S1), the copy number and genomic positions (Supplemental Tables S1, S2), and the correctness of the reading frame of the APOBEC gene in the integrated cassettes (Supplemental Fig. S2).

Upon doxycycline treatment, mCherry fluorescence as well as APOBEC upregulation were clearly detected within 48 h (Fig. 1B,C). Here, we treated with 0.1 µg/mL and 3 µg/mL of doxycycline for low- and high-level induction, respectively. Gene expression levels of induced A3A or A3B ranged from 400 to 6000 transcripts per millions (TPMs), representing a several hundred-fold increase over endogenous levels (Fig. 1D; Supplemental Fig. S3). Of note, endogenous APOBEC transcripts minimally contributed <0.2% of the total APOBEC transcripts (Supplemental Table S3).

Single-cell transcriptome data from various cancer types indicated that the range of APOBEC expression levels observed in our models were comparable to those observed during episodic bursts in many cancer types, including lung adenocarcinoma, head-and-neck squamous cell carcinoma, triple-negative breast cancer, esophageal adenocarcinomas, and squamous cell carcinomas (Supplemental Fig. S4; Puram et al. 2017; Karaayvaz et al. 2018; Wu et al. 2018; Maynard et al. 2020). Unfortunately, expression levels in gastric adenocarcinoma could not be explored due to the lack of available single-cell Smart-seq data.

Following A3A or A3B induction, the viability of the organoid lines was substantially compromised, suggesting a detrimental impact of APOBEC upregulation on cell survival (Fig. 1E). After APOBEC induction, differentially expressed genes included those involved in the cell cycle (e.g., *CDKN1A* and *CDC20*) and immune

response (e.g., *CXCL8* and *CCL20*) in both the hGO_{IA3A} and hGO_{IA3B} models (Fig. 1F; Amador et al. 2007; Wu et al. 2007; Cazzalini et al. 2010; Matsushima et al. 2022). The induced APOBEC enzymes predominantly localized to the nuclei and led to an increase in γ-H2AX foci, suggesting APOBEC-induced DNA damage, such as replication stalling or double-strand breaks (DSBs), as previously reported (Fig. 1G,H; Supplemental Fig. S5; Burns et al. 2013; Green et al. 2016).

APOBEC3A, not APOBEC3B, induces genomic mutations

To assess the mutagenic impacts of A3A and A3B, we investigated acquired mutations in the hGO_{IA3A} and hGO_{IA3B} lines after 48 h of doxycycline treatment. On average, the hGO_{IA3A} lines treated with 0.1 µg/mL and 3 µg/mL doxycycline exhibited 267 and 2448 SBS2/13 base substitutions genome-wide, respectively (0.1 µg/mL: 95% CI, 107–505; 3 µg/mL: 95% CI, 1052–3708) (Fig. 2A,B,F; Supplemental Tables S4, S5). In contrast, the hGO_{IA3B} clones showed a negligible number of APOBEC-associated mutations following induction (0.1 µg/mL: 95% CI, 0–1) (Fig. 2A,D,F; Supplemental Tables S4, S5).

To minimize potential detection bias in our single-cell cloning system, where proliferative cells are preferentially sequenced, we employed duplex DNA sequencing (Hoang et al. 2016), which precisely captures nonclonal mutations across the entire cell population, including those confined to single cells that could not proliferate further. The mutational burden per diploid genomes from the duplex DNA sequencing revealed a time-dependent increase in A3A-associated mutations following doxycycline treatment, ultimately resulting in higher levels than those observed from the clones (0.1 µg/mL: 95% CI, 4590–6038; 3 µg/mL: 95% CI, 9316–10,077) (Fig. 2A,C; Supplemental Table S6). In contrast, but in line with our observation on the clones, APOBEC-associated base substitutions in hGO_{IA3B} lines remained minimal in duplex sequencing (0.1 µg/mL: 95% CI, 136–352; 3 µg/mL: 95% CI, 79–133) (Fig. 2A; Supplemental Table S6). Of note, unlike hGO_{IA3A}, we did not detect A3B-associated mutations even at earlier time points (Fig. 2E), suggesting that the absence of mutations in hGO_{IA3B} is unlikely to be due to the negative selection against hypermutated cells. Our findings overall indicate that A3B alone does not act as a major mutator, at least in human normal gastric epithelium.

Despite the absence of fixed mutations in hGO_{IA3B} models, the A3B enzyme in cell lysates was fully functional, exhibiting strong cytosine deamination activity for extracellular DNA oligonucleotides in vitro (Fig. 3A). Denatured genomic DNA fragments exposed to recombinant A3B enzymes underwent near-complete deamination of unmethylated (non-CpG) cytosines ([~99%]) upon contact with the enzyme (Fig. 3B,C). This activity was further confirmed in the duplex DNA sequencing, where lysates from hGO_{IA3B} induced a substantial number of C>T artifacts during library preparation, particularly in the 5' head region (~50 bp) of the sequencing reads with a clear positive correlation with the doxycycline concentration, as reported previously (Supplemental Fig. S6A,B; Abascal et al. 2021). Finally, the increase in γ-H2AX foci in the hGO_{IA3B} following doxycycline induction (Fig. 1H; Supplemental Fig. S5) also indicates DNA damage consistent with A3B activity. Collectively, our findings strongly indicate that gastric organoids either efficiently repair A3B-induced lesions or possess intrinsic mechanisms that suppress A3B-associated cytosine deamination in the nucleus.

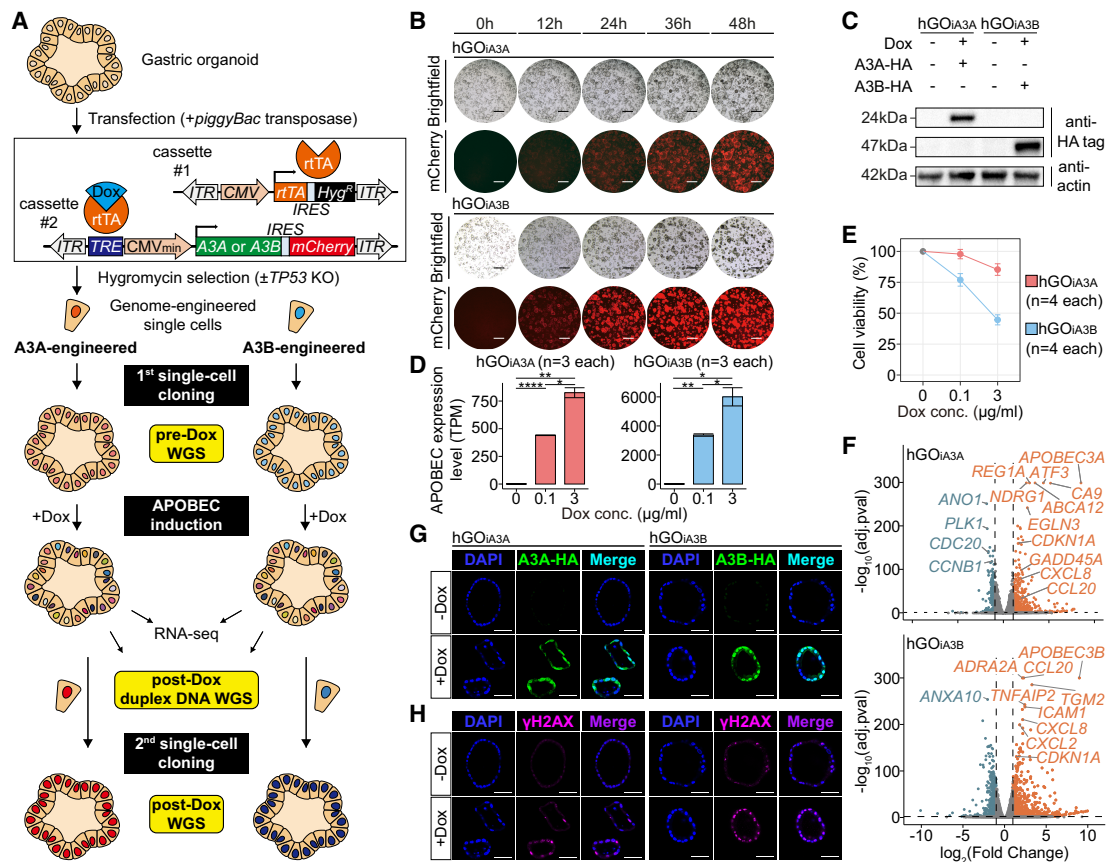


Figure 1. Overview of conditional APOBEC (APOBEC3A or APOBEC3B) overexpression models with human gastric organoids. (A) Experimental design of the study. Schematic illustration of genetic engineering, cloning, and sequencing (whole-genome sequencing, duplex sequencing, and bulk RNA-seq) is shown. Dox, doxycycline. (B) Changes of morphology and mCherry fluorescence during 48 h with 0.1 $\mu\text{g/ml}$ doxycycline treatment; (top) hGO_{iA3A} lines, and (bottom) hGO_{iA3B} lines. Scale bars represent 1 mm. (C) Inducible expression of APOBEC3A (A3A) or APOBEC3B (A3B) enzymes in hGO_{iA3A} and hGO_{iA3B} lines, respectively, following 3 $\mu\text{g/ml}$ doxycycline treatment for 48 h. (D) Expression levels of APOBEC3A (A3A) or APOBEC3B (A3B) in each line following 0.1 $\mu\text{g/ml}$ and 3 $\mu\text{g/ml}$ doxycycline treatment for 48 h; (left) hGO_{iA3A} lines (n = 3 per condition), and (right) hGO_{iA3B} lines (n = 3 per condition). Data are presented as mean \pm 95% confidence interval. Statistical significance was determined using a *t*-test: (*) $P < 0.05$, (**) $P < 0.005$, (****) $P < 0.00005$. (E) Changes of viability of each line following 0.1 $\mu\text{g/ml}$ and 3 $\mu\text{g/ml}$ doxycycline treatment for 48 h (n = 4 per each condition). Data are presented as mean \pm 95% confidence interval. (F) Differentially expressed genes upon APOBEC (A3A or A3B) overexpression following 0.1 $\mu\text{g/ml}$ doxycycline treatment for 48 h; (top) hGO_{iA3A} line, and (bottom) hGO_{iA3B} line. adj.pval, adjusted *P*-value. (G) Subcellular localization of overexpressed A3A and A3B following 3 $\mu\text{g/ml}$ doxycycline treatment for 48 h in each line; (left) hGO_{iA3A} line, and (right) hGO_{iA3B} line. Scale bars represent 50 μm . (H) γ -H2AX foci following 3 $\mu\text{g/ml}$ doxycycline treatment for 48 h in each line; (left) hGO_{iA3A} line, and (right) hGO_{iA3B} line. Scale bars represent 50 μm .

To further investigate whether inactivation of tumor suppressor genes accelerates APOBEC-associated mutagenesis, we generated the hGO_{iA3A} and hGO_{iA3B} lines carrying biallelic truncating mutations in *TP53* (hereafter referred to as *TP53KO*-hGO_{iA3A} and *TP53KO*-hGO_{iA3B}, respectively) (Fig. 1A). In the *TP53KO*-hGO_{iA3A} lines, we observed a similar burden of APOBEC-associated mutations as that observed in the hGO_{iA3A} lines (0.1 $\mu\text{g/ml}$: 95% CI, 785–1917; 3 $\mu\text{g/ml}$: 95% CI, 152–3091) (Fig. 2A,B; Supplemental Table S5). The *TP53KO*-hGO_{iA3B} lines exhibited a lack of APOBEC-associated mutations consistent with the hGO_{iA3B} lines (0.1 $\mu\text{g/ml}$: 95% CI, 11–19; 3 $\mu\text{g/ml}$: 95% CI, 2–12) (Fig. 2A,D; Supplemental Table S5). Taken together, these findings imply that the inactivation of *TP53* does not promote APOBEC-associated mutagenesis in gastric organoids.

Despite the increased γ -H2AX foci following A3A or A3B overexpression (Fig. 1H; Supplemental Fig. S5), which often indicate DNA DSBs, we did not observe a remarkable increase of structural variations (SVs) (Supplemental Table S5) in all the clones, including *TP53KO*-hGO_{iA3A} and *TP53KO*-hGO_{iA3B} lines. These findings

indicate that APOBEC-induced DSBs or replication stalls are efficiently repaired within gastric organoids.

Both APOBEC3A and APOBEC3B induce C > U RNA editing

Despite their contrasting mutagenic impact on DNA, both enzymes exhibited C > U RNA editing events. In RNA sequencing normalized to a total base count of 3.1Gb, both the hGO_{iA3A} and hGO_{iA3B} lines showed \sim eightfold and 30-fold increases in C > U RNA editing sites, following 0.1 $\mu\text{g/ml}$ and 3 $\mu\text{g/ml}$ doxycycline treatment for 48 h, respectively (Fig. 2G,I; Supplemental Fig. S7A; Supplemental Table S7).

The spectra of C > U RNA editing deviated from SBS2 associated with DNA mutations and also varied between A3A and A3B (Fig. 2H,J). Briefly, (1) both A3A and A3B exhibited reduced specificity for the UpCpU context (TpCpT in DNA). However, (2) A3A displayed enhanced specificity for the UpCpG context (TpCpG in DNA), and (3) A3B showed increased specificity for contexts other than UpCpN (non-TpCpN in DNA).

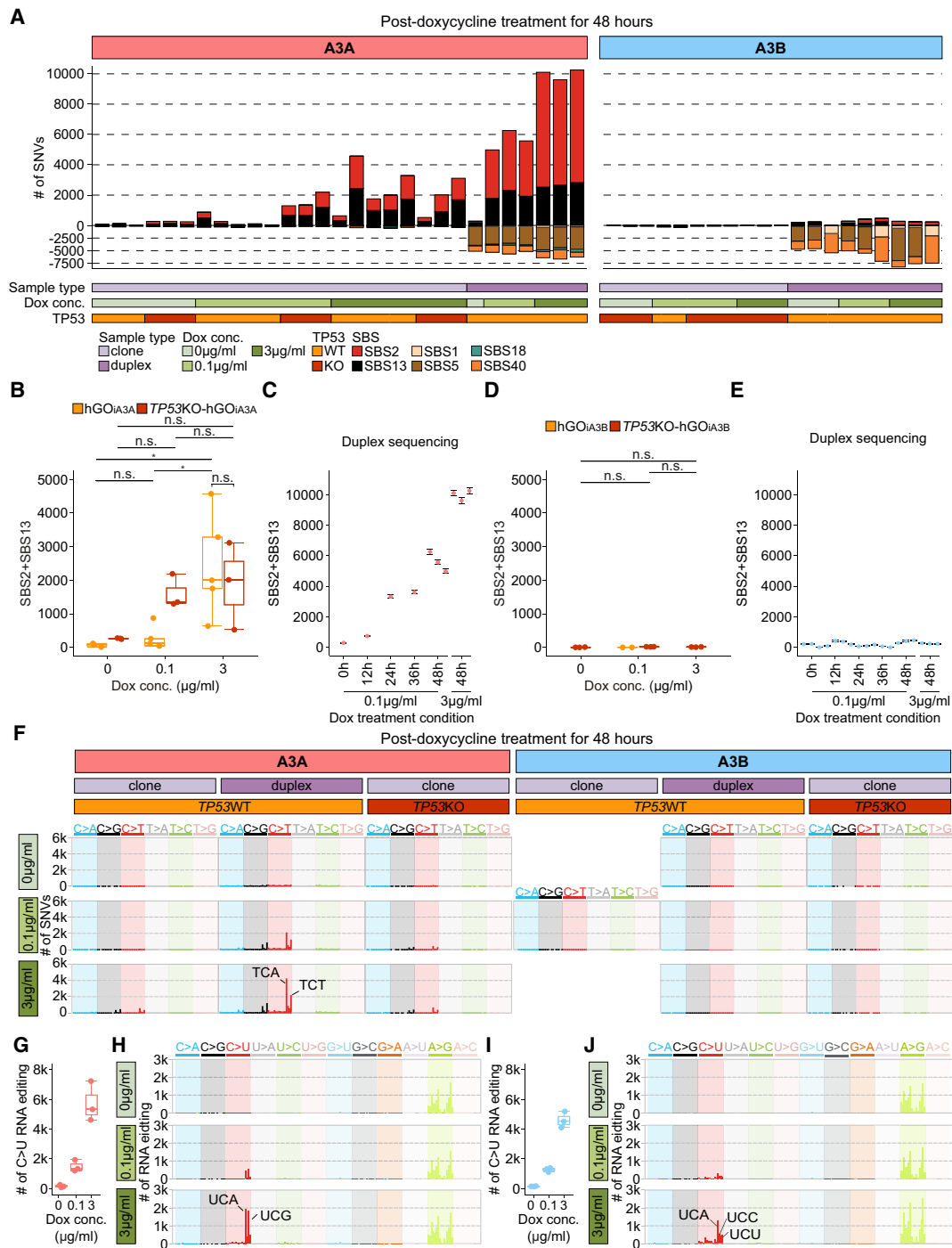


Figure 2. Mutational impact of APOBEC-associated single base substitutions in DNA and RNA. (A) Mutational burden of SNVs following APOBEC overexpression (A3A or A3B), measured by whole-genome sequencing of the clones and duplex DNA sequencing. The number of SNVs measured by the duplex DNA sequencing was normalized per diploid genome; (left) hGO_{IA3A} lines, and (right) hGO_{IA3B} lines. (B) Mutational burden of APOBEC-associated SNVs in the hGO_{IA3A} and TP53KO-hGO_{IA3A} clone sequencing. The number of A3A-associated SNVs (SBS2+SBS13) in hGO_{IA3A} and TP53KO-hGO_{IA3A} clones under each condition. Statistical significance was determined using a *t*-test: (*) *P* < 0.05, (n.s.) not significant. (C) Number of A3A-associated SNVs (SBS2+SBS13; normalized per diploid genome) in BotSeqS results for hGO_{IA3A} lines under each doxycycline treatment condition. Black lines represent 95% confidence intervals based on a Poisson distribution. (D) Mutational burden of APOBEC-associated SNVs in the hGO_{IA3B} and TP53KO-hGO_{IA3B} clone sequencing; the number of A3B-associated SNVs (SBS2+SBS13) in hGO_{IA3B} and TP53KO-hGO_{IA3B} clones under each condition. Statistical significance was determined using a *t*-test. (E) Number of A3B-associated SNVs (SBS2+SBS13; normalized per diploid genome) in BotSeqS results for hGO_{IA3B} lines under each doxycycline treatment condition. Black lines represent 95% confidence intervals based on a Poisson distribution. (F) Mutational burden and spectra of APOBEC-associated SNVs in each experimental condition. The number of SNVs in BotSeqS results were normalized per diploid genome; (left) hGO_{IA3A} lines, and (right) hGO_{IA3B} lines. (G) Number of C > U RNA editing in bulk RNA-seq in hGO_{IA3A} lines (*n* = 3 per condition), normalized per 3.1 Gb of mapped bases. (H) Spectra of RNA editing in trinucleotide contexts in hGO_{IA3A} lines. (I) Number of C > U RNA editing in bulk RNA-seq in hGO_{IA3A} lines (*n* = 3 per condition), normalized per 3.1 Gb of mapped bases. (J) Spectra of RNA editing in trinucleotide contexts in hGO_{IA3B} lines.

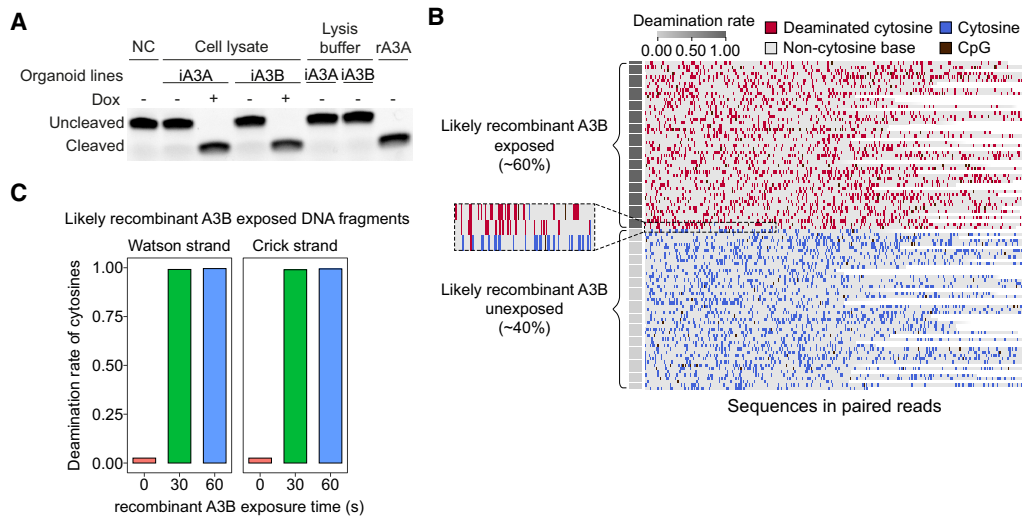


Figure 3. Deamination activity of APOBEC3B in vitro. (A) Cytosine deaminase activities of cell lysates from hGO_{IA3A} and hGO_{IA3B} lines following 3 μg/mL doxycycline treatment for 48 h. NC, negative control; rA3A, recombinant A3A. (B) Sequences in randomly selected 100 read pairs in recombinant APOBEC3B-exposed cell-free denatured genomic single stranded DNA for 60 sec. (C) Deamination rate of unmethylated cytosines in recombinant A3B-exposed cell-free DNA fragments. 0, negative control; 30, DNA exposed for 30 sec; 60, DNA exposed for 60 sec.

Further de novo decomposition of RNA editing spectra revealed three RNA editing signatures, referred to as RNA-SBS_A, RNA-SBS_B, and RNA-SBS_C, corresponding to A3A-, A3B- and adenosine deaminase RNA specific (ADAR)-associated A-to-I RNA editing, respectively (Supplemental Fig. S8A,B). Although RNA-SBS_A was overall consistent with an A3A-associated RNA-editing spectrum previously reported (Martínez-Ruiz et al. 2023; Fixman et al. 2024), RNA-SBS_B was slightly different from one for A3B established from *Mus musculus* (Alonso de la Vega et al. 2023). Spectra in pentanucleotide contexts further showed that A3A-associated RNA editing was preferentially enriched in ApUpCpApN (ApTpCpApN in DNA) and ApUpCpGpN (ApTpCpGpN in DNA) contexts, whereas A3B-associated editing did not show such an enrichment (Supplemental Fig. S9).

The C>U RNA editing sites were frequently recurrent, particularly among the sites identified in the low doxycycline concentration (Supplemental Fig. S7B). Of the 16,574 C>U RNA editing sites detected across all samples, 7593 (45.8%) were recurrent or observed in more than one sample (Supplemental Fig. S7C–E; Supplemental Table S8), suggesting that these were C>U RNA editing hotspots. Of these, 3769 and 2769 were exclusively identified in hGO_{IA3A} and hGO_{IA3B} lines, respectively (Supplemental Fig. S7D,F).

A3A-associated RNA editing hotspots were enriched in specific sites in the secondary stem-loop structure of RNAs, including the 3rd, 4th, and 4th positions of the 3-bp, 4-bp, and 5-bp RNA-loop structures, respectively, as reported previously (Supplemental Fig. S7G; Jalili et al. 2020). Further, we found an enrichment in specific positions of the larger loops (Supplemental Fig. S7G). In contrast, A3B-associated RNA editing hotspots did not show site preferences in the RNA-loop structures (Supplemental Fig. S7G). The lower context stringency in A3B may be caused by the structural differences of α 1/loop-1 and β -2 residues of the CD2 domain (Kim et al. 2023).

Characteristics of APOBEC-associated mutations

Using the pure A3A-mediated mutational profiles from hGO_{IA3A} lines, we examined the detailed characteristics of A3A-associated

mutational signatures. These analyses could not be applied to A3B due to the near absence of A3B-associated mutations in this study (Supplemental Fig. S10A–C). A3A-associated mutations in the TpCpA context were 2.7× more abundant following pyrimidine bases (YpTpCpA) compared to purine bases (RpTpCpA) (Fig. 4A). Of note, the RpTpCpA sequence context has been reported as a preferred motif for A3B-associated mutations in the *Saccharomyces cerevisiae* and in vitro model (Chan et al. 2015; Sanchez et al. 2024). The YpTpCpA preference in our study closely mirrors the enrichment level observed in human cancer tissues carrying APOBEC-induced hypermutations (YpTpCpA/RpTpCpA = 2.5 in cancers with SBS2/13 burdens >5000 genome-wide), indicating that A3A could be a key enzyme of the APOBEC-associated hypermutations in most human cancers.

Further, in line with previous reports from cancer (DeWeerd et al. 2022), indels attributable to the COSMIC ID9 signature (Sondka et al. 2024) showed a suggestive positive correlation with the number of A3A-associated base substitutions in hGO_{IA3A} clones, one per 333 SBS2/13 base substitutions (*P*-value = 0.051) (Fig. 4B). Of note, base substitutions attributable to clock-like mutational signatures (SBS5 and SBS40) demonstrated a positive correlation with the burden of A3A-associated base substitutions (SBS2 and SBS13) (Fig. 4C), suggesting that A3A-induced genomic damage indirectly promotes error-prone DNA repair processes across the genome. However, this association was absent in hGO_{IA3A} clones carrying TP53 truncating mutations (Fig. 4C). We speculate that this difference reflects differential DNA repair pathways according to the activities of TP53 (Kim et al. 2016). Notably, among the polymerases encoded in the human genome, increased transcription of DNA polymerase eta (*POLH*), which is involved in translesion synthesis (TLS) (Choi and Pfeifer 2005; Delbos et al. 2005), was exclusively observed in clones with functional TP53 (Fig. 4D; Supplemental Fig. S11). Previously, *REV1*, a component of the TLS pathway, was shown to contribute to the generation of SBS5 and SBS40 in cancer cell lines (Petljak et al. 2022). Collectively, this suggests that the TLS machinery may contribute to the mutational processes underlying SBS5 and SBS40.

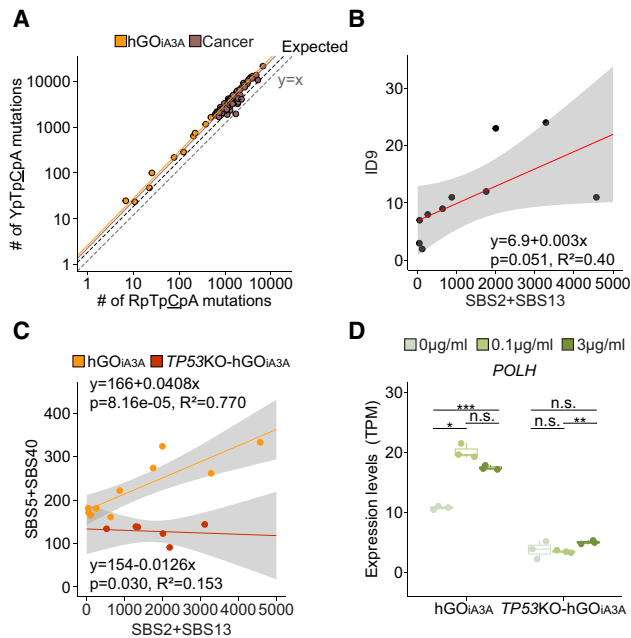


Figure 4. Characteristics of A3A-associated mutational signatures. (A) Context preference of A3A between YpTpCpA and RpTpCpA context in hGO_{iA3A} lines and APOBEC-associated mutations in hypermutant cancer samples. Only PCAWG cancer samples with a combined APOBEC-associated clonal mutational burden (SBS2+SBS13) greater than 5000 were selected ($n=63$) among eight cancer types with a high prevalence of APOBEC mutational activity: lung adenocarcinoma ($n=15$), breast adenocarcinoma ($n=12$), bladder urothelial carcinoma ($n=11$), head-and-neck squamous cell carcinoma ($n=13$), lung adenocarcinoma ($n=6$), uterine corpus endometrial carcinoma ($n=3$), esophageal adenocarcinoma ($n=2$), and stomach adenocarcinoma ($n=1$). Dashed black line, expected; orange line, hGO_{iA3A}; dark brown line, cancer. (B) Correlation between A3A-associated base substitutions and ID9 contributing indels among hGO_{iA3A} lines. (C) Associations between A3A-associated (SBS2 and SBS13) and age-associated (SBS5 and SBS40) SNVs among hGO_{iA3A} lines and TP53KO-hGO_{iA3A} clones. (D) Changes in *POLH* gene expression (translesion synthesis DNA polymerase) following A3A induction in hGO_{iA3A} and TP53KO-hGO_{iA3A} lines.

Clusters of APOBEC-associated mutations

In cancer genomes, APOBEC-induced localized hypermutation events are frequently observed (Nik-Zainal et al. 2012a; The ICGC/TCGA Pan-Cancer Analysis of Whole Genomes Consortium 2020). Across the mutations detected in our hGO_{iA3A} and TP53KO-hGO_{iA3A} lines, ~5% of the 29,650 acquired base substitutions were clustered within 1 kbp, which is ~100-fold higher than expected by chance (Fig. 5A). Such clustered mutation events can be classified as either *omikli* and *kataegis*, based on the density (Bergstrom et al. 2022b). Overall, we detected 615 *omikli* and 109 *kataegis* events. The observed *kataegis* events ranged from four to 22 base substitutions (median = 5). The absence of correlation between the clustered mutations in this study and complex genomic events indicate that those were driven by the pure activity of A3A. For instance, SV-associated *kataegis*, which consists of ~36% of *kataegis* events in cancer genomes (Nik-Zainal et al. 2012a; The ICGC/TCGA Pan-Cancer Analysis of Whole Genomes Consortium 2020; Bergstrom et al. 2022b), were rare in our data (2.8%; 3 out of 109 events). Similarly, the *kataegis* in our clones were independent of other known *kataegis*-inducing genomic events, such as anaplastic DNA bridges (Maciejowski et al. 2020) and extrachromosomal DNA (ecDNA) (Bergstrom et al. 2022b).

The relative frequencies of *omikli* and *kataegis* remained consistent at 2.4% (95% CI: 1.7%–3.1%) and 0.4% (95% CI: 0.22%–0.58%) of all A3A-associated mutation events, respectively, with each isolated and clustered mutation counted as a single event (Fig. 5B; Supplemental Table S9). These ratios were more or less constant among clones, regardless of the doxycycline concentration or TP53 mutational status. Notably, the frequencies of *omikli* and *kataegis* were comparable to the SV-unrelated *omikli* and *kataegis* frequencies in cancers (Fig. 5B; Supplemental Table S9).

Within *kataegis* regions, cytosine alterations did not always occur in the TpCpN context. We observed that ~7% of cytosine substitutions occurred in non-TpCpN context (39 out of 556 mutations) (Fig. 5C), about twofold higher than expected on SBS2 and SBS13 signatures (7.00% vs. 3.33%; χ^2 test, $P < 0.005$). Our data indicated that these non-TpCpN mutations are not independent but are part of *kataegis* for two reasons: (1) non-TpCpN mutations were 267-fold more abundant than observed in the background regions (Fig. 5D); and (2) non-TpCpN mutations within *kataegis* regions were completely phased with other classical TpCpN mutations on the same allele (27 out of 27), where only 50% phasing would be expected by chance. This suggests that DNA repair mechanisms for cytosine deamination in non-TpCpN contexts are less accurate in the mutagenesis of clustered mutations.

Of the 615 *omikli* and 106 *kataegis* events (excluding three *kataegis* events associated with rearrangements), ~5% (35 *omikli* and 5 *kataegis* events) exhibited strand-switching of the mutated cytosines between parental and daughter strands during replication (Fig. 5E,F). In one *kataegis* event, composed of nine base substitutions (in clone A3A_1st_C3_3μg-5), we observed five strand-switching events (Fig. 5G). Phasing analysis revealed that clustered mutations on both DNA strands occurred on the same allele (26 out of all 26 informative events). Additionally, the mutational spectrum of the minorly contributing strand was predominantly composed of mainly C>T or C>G mutations in the TpCpN context (62%; 13 out of 21 mutations) (Fig. 5C), implying that all the mutations were APOBEC-associated. Besides, the rate of TpCpN mutations in the minor strand within strand-switching *kataegis* regions was 124-fold higher than randomly expected (Fig. 5H). Although the underlying mechanism remains unclear, our findings indicate that strand-switching of the A3A enzyme should be possible when generating clustered mutations during replication (Fig. 5F).

Epigenetic contexts associated with A3A-associated mutations

Mutational processes are often influenced by the epigenetic contexts of the genome (Otlu et al. 2023). Of the 14 genomic features examined, three features (replication timing, local transcription level, and H3K27me3) showed potential associations with local A3A-associated mutational burdens (Fig. 6A). Of the three features, replication timing and local gene transcription level demonstrated consistent trends correlating with A3A-associated mutation rates (Supplemental Table S10).

For the replication timing, the latest-replicating regions showed a 1.26-fold higher rate of A3A-associated mutation compared to the earliest-replicating regions (Fig. 6B) as previously reported (Kazanov et al. 2015). This may be attributed to the DNA repair mechanisms, including base excision repair, which are particularly active in early-replicating regions consisting of open chromatin (Amouroux et al. 2010; Rhind and Gilbert 2013). Further, the A3A-associated mutation rate in the lagging strand of DNA replication was 1.26-fold higher compared to the leading strand

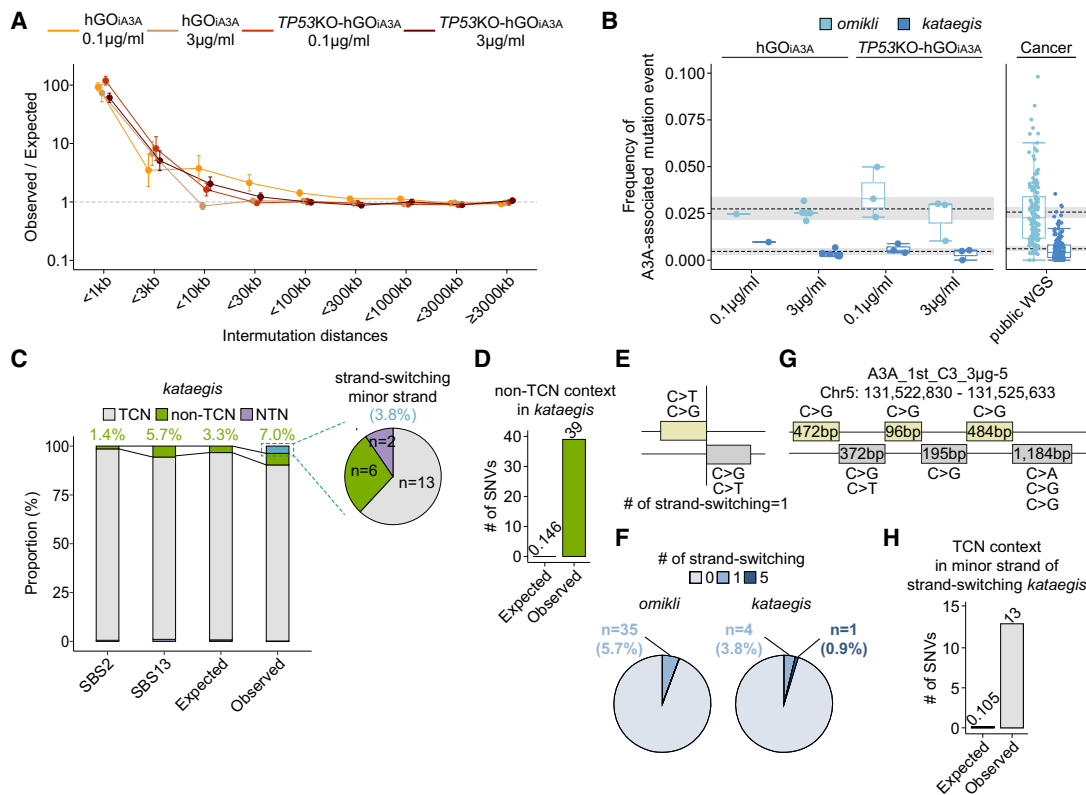


Figure 5. Landscape of APOBEC3A-associated clustered mutation. (A) Observed-to-expected ratios of the intermutational distances between SNVs in each clone. Data are presented as mean \pm standard error. (B) Frequencies of clustered mutation events (*omikli* and *kataegis*) among A3A-associated base substitutions in clones and cancer genomes. (C) Proportions of classic (in TpCpN context) and nonclassical mutations (in non-TpCpN and NpTpN) in SBS2, SBS13, and *kataegis* regions in the clones. (D) Comparison of expected and observed number of SNVs in the non-TpCpN context within *kataegis* regions. (E) Schematic representation of strand-switching *kataegis*. (F) Strand-switching frequencies of *omikli* and *kataegis* across classes of clustered mutation events. (G) A complex strand-switching *kataegis* involving five switches found in clone A3A_1st_C3_3µg-5. (H) Enrichments of minor strand mutations in the TpCpN context in strand-switching *kataegis* events.

(Fig. 6C), which presumably originated from more frequent exposure of single-stranded DNA (ssDNA) induced by Okazaki fragments in the lagging strand (Wu et al. 2020), similar to previous elucidation (Hoopes et al. 2016). In addition, mutation rates in genic regions were correlated with expression levels (Fig. 6D), showing a 1.37-fold higher mutation rate in actively transcribed genomic regions compared to silent genic regions, consistent with the previous studies (Nordentoft et al. 2014; Kazanov et al. 2015). Of note, the lagging strand and highly transcribed genes tend to be more frequently single-stranded than the leading strand and silent genes (Okazaki et al. 1968; Gnatt et al. 2001), which may make them more susceptible to A3A-induced DNA damage, respectively. The results demonstrated that DNA regions with frequent ssDNA exposure have a higher chance of being damaged by A3A. In line with this observation, the nontranscribed genic strand was mutated 1.13-fold more frequently than the transcribed strand (Fig. 6E), consistent with a previous report (Saini et al. 2017).

Compared with noncoding sequences, protein-coding sequences showed much lower mutation rates, at 0.79-fold the genome average, suggesting a selective pressure against mutations that could alter amino acid-changing mutations (Fig. 6F). Of note, in TP53-inactivated clones (TP53KO-hGO_{iA3A} clones), mutation rates in protein-coding regions slightly increased to 0.834-fold of the genome average, potentially due to reduced negative selection pressures in the absence of functional TP53.

Discussion

Our study clearly demonstrated the qualitative and quantitative mutational impact of A3A and A3B in human non-neoplastic cells using a gastric organoid culture system. Previous studies have highlighted the mutagenic potential of A3B in various model systems (Chan et al. 2015; Carpenter et al. 2023; Durfee et al. 2023; Dananberg et al. 2024). In contrast, a recent study suggested only a modest contribution of A3B mutagenesis in human cancer cell lines (Petljak et al. 2022). To our knowledge, our study is the first to directly assess the mutagenic activity of A3B in human normal cells.

The gastric organoid model offered distinct advantages based on three key criteria: (1) biological relevance, supported by the frequent occurrence of APOBEC-associated mutations in gastric cancers; (2) experimental feasibility, owing to its robust proliferative capacity under culture conditions; and (3) the availability of standardized protocols for genetic manipulation (Fujii et al. 2015; Gaebler et al. 2020). For example, despite the high prevalence of APOBEC-associated mutations in breast and lung cancers, the corresponding normal epithelial cells are suboptimal for this study due to their limited proliferative capacity in organoid culture as well as their poor compatibility with genetic engineering.

When A3A was induced by 3 µg/mL of doxycycline in hGO_{iA3A} lines, transcription was activated for ~2–3 days, reaching

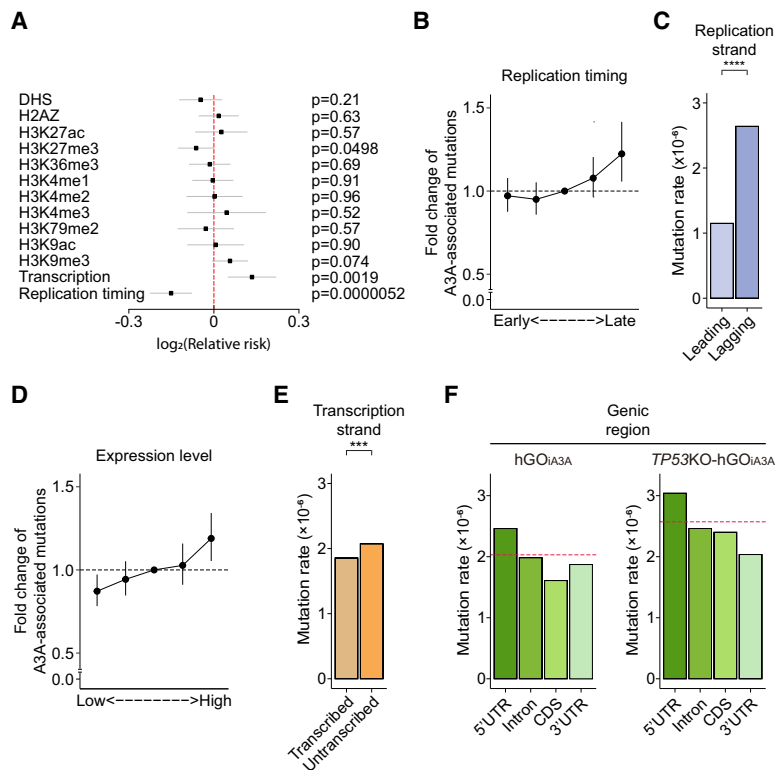


Figure 6. Genomic and epigenomic distribution of APOBEC3A-associated mutations. (A) Correlations between epigenetic markers and A3A-associated substitutions. (B) Fold change of mutation rates of A3A-associated SNVs across genomic regions grouped by replication timing. Data are presented as mean \pm 95% confidence interval. (C) Mutation rates on the leading and lagging DNA strands during replication. Statistical significance was determined using a χ^2 test: (****) $P < 0.00005$. (D) Fold change of mutation rates of A3A-associated SNVs across genomic regions grouped by transcription. Data are presented as mean \pm 95% confidence interval. (E) Mutation rates on the transcribed and untranscribed DNA strands during transcription. Statistical significance was determined using a χ^2 test: (****) $P < 0.0005$. (F) Mutation rates across subgenomic regions (5'-UTR, introns, protein coding sequences [CDSs], and 3'-UTR) in hGO_{IA3A} clones (left) and TP53KO-hGO_{IA3A} clones (right). Red dashed line, average genome-wide mutation rate.

peak expression levels of ~ 800 TPM. Under these conditions, we detected ~ 2500 A3A-induced base substitutions in proliferative clones, suggesting that ~ 1000 base substitutions could be acquired in a day. These findings support the notion that a transcriptional burst of A3A can also lead to a massive number of mutations in normal gastric epithelium as well, consistent with previous observations in cancer (Petljak et al. 2019). However, the frequency of episodic A3A upregulation per se is unknown in human normal gastric epithelium. According to conventional wisdom, APOBEC overexpression is thought to be associated with viral infection. However, publicly available transcriptomic data from SARS-CoV-2-infected human gastric organoids revealed no substantial upregulation of A3A or A3B (Supplemental Fig. S12; Giobbe et al. 2021).

Our models also indicated increased mutational burdens of SBS5 and SBS40 proportional to the overall burden of A3A-associated mutations, suggesting that base substitutions attributable to other than SBS2 and SBS13 can also be indirectly promoted in APOBEC upregulation. These signatures were significantly enriched in late-replicating regions and correlated with multiple epigenomic features, including replication timing and transcriptional activity, in line with previous reports (Supplemental Fig. S13A,B; Sondka et al. 2024).

Although this study successfully evaluated the mutagenic activity of A3A and A3B in human normal cells, several technical

limitations warrant consideration. First, the study was primarily conducted using gastric epithelial cells, and we cannot exclude the possibility that A3B may exhibit substantial mutagenic activity in other cell types. Second, the endogenous copies of A3A and A3B were not inactivated in the hGO_{IA3A} and hGO_{IA3B} models, raising the possibility that a minor fraction of the observed APOBEC-associated mutations and RNA editing sites may have originated from native enzymes. Third, the inclusion of additional control models, such as catalytically inactive mutants (e.g., A3A-E72A and A3B-E255A) (Carpenter et al. 2023) or APOBEC-enzyme inhibitors, would further clarify the mechanisms underlying APOBEC overexpression. Finally, our genomic analyses were conducted using an earlier version of the human reference genome (GRCh37), due to the dependency of our somatic mutation calling pipeline using previously constructed large-scaled unmatched normal sample matrix based on the GRCh37 sequences (Park et al. 2021). Nonetheless, our findings remain consistent in the benchmark analysis with the latest reference (GRCh38) (Supplemental Fig. S14).

Methods

Material availability

Organoids established in this study will be available under a material transfer agreement. To do so, please contact the lead author (ysju@kaist.ac.kr).

Human normal gastric samples

Normal gastric tissues were obtained via endoscopic biopsy from a female undergoing routine screening. The protocol for this study was approved by the Institutional Review Board of Yonsei University Gangnam Severance Hospital (3-2018-0207) and KAIST (KH2022-211).

Human stomach organoid culture

Organoid culture methods and media compositions were adopted from previous research with slight modifications (Bartfeld et al. 2015). Wnt3A- and R-Spondin 1-conditioned media were produced with the HEK293 cell line producing Afamin-Wnt3a (Mihara et al. 2016) and the Cultrex HA-R-Spondin 1-Fc 293T cell line (Trevigen, #3710-001-01).

Tissues were incubated in TrypLE (Gibco, #12604013) at 37°C for 30 min, then dissociated into clusters of 10–15 cells by pipetting. After washing with PBS twice and centrifugation at 300g for 5 min at 4°C, pellets were resuspended in cold Matrigel (Corning, #BDL356231) and seeded in 12- or 24-well plates (Merck). Following a 10-min incubation at 37°C in 5% CO₂, 0.5–1 mL of prewarmed culture medium was added. Medium was changed every 2–3 days. Organoids were passaged every 2 weeks using Cell

Recovery solution (Corning, #354253) and Accutase (Stemcell Technology, #07922) (see Supplemental Methods; Supplemental Table S11).

Preparation of vectors for transfection

Two vectors were purchased: (1) *CMV-rtTA-Hyg^R* vector (Addgene, #102423) and (2) CRISPR-*Cas9* vectors containing gRNA sequence for *TP53* (Addgene, #121917). To generate the *pPB-CMVmin-APOBEC (A3A or A3B)-IRES-mCherry* vectors, either the APOBEC3A (NM_145699.4) or APOBEC3B (NM_004900.4) sequence was cloned into the vector backbone containing a Tet-on system (*pPB-TRE-CMVmin-IRES-mCherry*) (see Supplemental Methods; Lee et al. 2022).

Transfection of organoids

Transfection methods were adopted from previously reported protocols (Fujii et al. 2015; Gaebler et al. 2020). A mixture of three kinds of vectors was utilized: (1) *pPB-TRE-APOBEC (A3A or A3B)-IRES-mCherry*; (2) *pPB-CMV-rtTA-Hyg^R*; and (3) *piggyBac* transposase. Organoids resuspended in Opti-MEM (Gibco, #31985062) or BTXpress buffer (BTX) were mixed with a vector cocktail. Electroporation was performed using a previously described program from the literature (see Supplemental Methods; Supplemental Table S12; Fujii et al. 2015). Selection was carried out for 1 week with 1 μ g/mL hygromycin (InvivoGen, #ant-hg-1). Single-cell cloning was performed using FACSARIAII (BD Biosciences), followed by manual picking of organoids derived from single cells by pipetting (Youk et al. 2021).

Doxycycline treatment

A doxycycline (Sigma-Aldrich, #D9891-1G) stock solution was prepared by dissolving doxycycline in DMSO. Prior to treatment, dissociated 10k viable cells were seeded in 24-well plates. After 7 days, doxycycline solution was added to the medium, and the organoids were incubated with doxycycline.

Capturing fluorescent images

mCherry fluorescence following doxycycline treatment was visualized using a fluorescence microscope (LEICA, DMi8). Fluorescent images were captured using Las X programs, and brightness/contrast adjustments were applied using the same program.

Preparation of cell lysates

Organoids treated with 3 μ g/mL doxycycline were harvested using Cell Recovery solution (Corning), followed by one wash with PBS. The isolated cell pellets by centrifugation were resuspended in lysis buffer containing 25 mM HEPES (pH 7.9), 10% glycerol, 150 mM NaCl, 0.5% Triton X-100, 1 mM EDTA, 1 mM MgCl₂, 1 mM ZnCl₂, RNase A (0.2 mg/mL; Thermo Fisher Scientific, #EN0531), and 1 \times protease inhibitors (Thermo Fisher Scientific, #877885). Cell lysates were then sonicated, incubated on ice for 30 min, and centrifuged at 13,000 rpm at 4°C for 10 min. The supernatant was collected, and protein concentration was measured with Qubit Protein and Protein Broad Range (BR) Assay kits (Thermo Fisher Scientific, #Q33211).

Western blotting

Lysates were prepared by mixing samples 1:1 with Laemmli Sample Buffer (Bio-Rad, #161-0737), followed by denaturation at 95°C for 5 min. Proteins were separated by SDS-PAGE on a Mini-PROTEAN TGX pre-cast 12% gel (Bio-Rad, #4561044) in SDS

running buffer (Higene, #PB151-10h) and transferred to an Immobilon PVDF membrane (Millipore, #IPFL00010) via overnight wet transfer in Tris/Glycine buffer (Bio-Rad, #1610771).

Primary antibodies included anti-HA.11 Epitope Tag Antibody (1:5000; BioLegend, #951514) and anti- α -Actin-1 (1:1000; Sigma-Aldrich, #A2066). HRP-conjugated secondary antibodies were used at 1:2000 dilution: goat anti-mouse IgG-HRP for anti-HA (Santa Cruz, #sc-2005) and goat anti-rabbit IgG-HRP for anti-actin (Santa Cruz, #sc-2004) (see Supplemental Methods).

Whole transcriptome sequencing library construction

RNA was isolated during DNA extraction for BotSeqS libraries with AllPrep DNA/RNA Mini kit (QIAGEN, #80204), following the manufacturer's instructions. Libraries were constructed with the NEBNext Ultra II Directional DNA Library Prep kit for Illumina (NEB, #E7760) and the QIAseq FastSelect -rRNA HMR kit (QIAGEN, #334388), according to the manufacturer's instructions. Libraries were sequenced on the NovaSeq 6000 with paired-end sequencing.

Calculating RNA expression levels

Bulk RNA-seq reads were aligned to GRCh37 using STAR2 v2.6.1d (Dobin et al. 2013). TPM and read counts were calculated with RSEM v1.3.1 (Li and Dewey 2011). Differential expression gene analysis was conducted using the DESeq2 package in R (Love et al. 2014).

Calculation of the ratio between endogenous APOBEC mRNA and overexpressed APOBEC mRNA

Sequence differences between the endogenous and overexpressed mRNA were utilized for counting (see Supplemental Methods). The proportion of endogenous mRNA was estimated by calculating the ratio of supporting reads.

Analysis of APOBEC3A and APOBEC3B expression levels in single cancer cells with public scRNA data

Publicly available single-cell RNA-seq data sets, generated with a Smart-seq library, from lung adenocarcinoma, triple negative breast cancer, esophageal adenocarcinoma, and esophageal squamous cell carcinoma were analyzed using the same pipeline applied to our bulk RNA-seq data. Epithelial cell populations were first identified following the tutorial workflow of the Seurat R package (Satija et al. 2015), without applying a cell filtering step. Within the epithelial population, cancer cells were distinguished based on the presence of large-scale copy number variations (CNVs) inferred using the inferCNVpy Python package (<https://infercnvpy.readthedocs.io/en/latest/index.html>). CNV profiles were calculated using fibroblast and endothelial cell populations as reference nonmalignant cells. For the head-and-neck squamous cell carcinoma data set, where raw data were not available, we utilized a publicly provided summary table containing TPM values and annotated cell types.

Viability assay of organoids

Organoid viability was assessed using the Celltiter-Glo 3D Assay kit (Promega, #G9681), following the manufacturer's instructions (see Supplemental Methods). Viability was calculated as the percentage of luminescence in doxycycline-treated samples related to the average luminescence of control groups.

Immunostaining and imaging of organoids

Whole-mount staining of human gastric organoids was performed as previously described (van Ineveld et al. 2020). Briefly, organoids were fixed with 4% paraformaldehyde (PFA) after depolymerizing the 3D matrix using ice-cold Cell Recovery solution (Corning). After washing with 0.1% PBS-Tween-20 and blocking with organoid washing buffer (0.1% Triton X-100, 0.02% SDS, 0.2% bovine serum albumin [BSA] in 1× PBS), immunolabeling was performed with mouse anti-HA tag antibody (1:50; Santa Cruz, #sc-7392) and rabbit anti-phospho-histone H2A.X antibody (1:400; CST, #2577S) to detect HA-tagged APOBEC proteins and DNA damage, respectively. Secondary antibodies included goat anti-mouse Alexa Fluor 488 (1:500; Thermo Fisher Scientific, #A-11001) and donkey anti-rabbit Alexa Fluor 647 (1:500; Thermo Fisher Scientific, #A32795). Nuclei were counterstained with DAPI (1:1000; Sigma-Aldrich, #D9542). After washing, FUnGI clearing solution was added to the organoids, which were then mounted between two coverslips with a 0.25-mm-deep iSpacer (SunJin Lab, #IS213). Imaging was performed at least 1 h after slide preparation. Imaging was performed with a Leica Stellaris 8 Confocal Microscope. Alexa Fluor 488, Alexa Fluor 647, and DAPI signals were obtained using either 40× or 63× objectives, with a digital zoom factor of one- to seven-fold. The X/Y resolution was set to 1024×1024 pixels. Images were processed and analyzed using Adobe Photoshop.

Standard whole-genome sequencing alignment

According to the manufacturer's protocol, DNA from clonal organoids was extracted using a DNeasy Blood & Tissue kit (QIAGEN, #69506), and libraries were constructed with TruSeq DNA PCR-Free Library Prep kits (Illumina, #20015963). Whole-genome sequencing was performed on the NovaSeq 6000 with a mean 30× depth of coverage. Adapter sequences in the FASTAQ files were removed by cutadapt software (Martin 2011). For WGS and BotSeqS, reads were aligned to the human reference genome GRCh37 using BWA-MEM v0.7.17 (Li and Durbin 2010). Further processing, including sorting, marking duplication, and indel realignment, was conducted with SAMtools v1.9 (Li et al. 2009), Picard v2.1.0 (McKenna et al. 2010), and GATK tools v3.8.0 (McKenna et al. 2010). For in vitro deamination results, Bismark v0.23.0 (<https://felixkrueger.github.io/Bismark/>) was utilized for the mapping process.

BotSeqS library construction

Libraries constructed with TruSeq DNA PCR-Free Library Prep Kit (Illumina) were utilized for the BotSeqS libraries construction. The construction of BotSeqS libraries was based on the previous literature with slight modifications (Hoang et al. 2016). Briefly, after the quantification of DNA libraries with the KAPA Library Quantification Kit Illumina Platforms (Roche, #KK48247), libraries equivalent to 4 pg of DNA were amplified with primers having a Y-adaptor sequence with a phosphorothioate bond(*) at the 3' end from IDT:

Forward: 5'-AATGATACGGCGACCACCGAG*A-3'
Reverse: 5'-CAAGCAGAAGACGGCATACGA*G-3'

PCR was performed for 20 cycles, following the protocol of the KAPA Library Amplification kit (Roche). Libraries were sequenced as paired-end sequencing (2×151 bps) on the NovaSeq 6000.

Calling copy number variations

Copy number variations were accessed by Sequenza (Favero et al. 2015). CNVs in segments smaller than 1 Mbp were considered

false-positives. After removing these short-segment CNVs, final CNV profiles were obtained through a second run of the Sequenza.

Confirming non-neoplasticity in primary human gastric organoid

Germline variant calling was performed using the germline mutation calling mode in GATK v4.0.12.0 (McKenna et al. 2010). The primary call set was first filtered using in-house scripts based on the pysam module in Python (Li et al. 2009). Given the relevance of cancer driver genes, the functional impact of variants was evaluated. The absence of CNVs in the normal gastric organoids was also confirmed (Supplemental Fig. S15).

Detection of somatic mutations

To detect single nucleotide variants and indels in clonal organoids, GATK Mutect2 v4.1.9 (McKenna et al. 2010) and Strelka2 v2.9.2 (Kim et al. 2018) were utilized. Bulk whole-genome sequencing of first single-cell cloned lines, hGO_{IA3A}, TP53KO-hGO_{IA3A}, hGO_{IA3B}, and TP53KO-hGO_{IA3B} organoids, were utilized as matched normal for calling somatic mutations in doxycycline-treated organoids. False-positive variants in each call set were filtered out with in-house Python scripts annotating information within BAM files with the pysam module (see Supplemental Methods). The filtered call sets from both Mutect2 and Strelka2 were merged, and the union call set was utilized for downstream analysis. To exclude mutations generated during the culture of first single-cell cloned lines, recurrent somatic mutations observed across multiple samples were removed.

For BotSeqS, VarScan2 v2.3.9 (Koboldt et al. 2012) was used to increase the sensitivity. Similarly, in-house Python scripts were utilized to remove false-positive calls (see Supplemental Methods). Unlike with standard whole-genome sequencing, over-expressed A3B induced the significantly increased C>T artifacts in the 5' head region during the BotSeqS library construction process (Supplemental Fig. S6A,B). Thus, the false-positive SNVs located within 100 bp of the 5' end or 3' end, considering reference strand, were removed. Additionally, rare variants from HEK293 cells, which were used to generate the conditioned medium, were observed. Thus, variants observed at least three times in the HEK293 BAM file were removed from the final call set.

Calculation of mutation rate in BotSeqS

Unlike standard WGS, the effective covered region was calculated for each BAM file. First, each read was evaluated using in-house scripts that considered DNA strand orientation and applied the following criteria to isolate effective DNA fragments: (1) median mapping quality >20; and (2) total depth of each type of reads ≥3. Only regions where both F1R2 and F2R1 reads were aligned were included in the covered region calculation. To account for the exclusion of mutations located within 100 bp of the extreme of read-ends during variant filtering (considering the reference genome strand), the total length of the covered region was adjusted by multiplying it by $[(151 \times 2 - 110) / (151 \times 2)]$. Mutation rates were calculated by dividing the number of observed mutations by this adjusted covered length. To normalize mutational burdens to the standard genome length, mutation rates were then multiplied by dividing the number of observed mutations by this adjusted covered length. To normalize mutational burdens to the standard genome length, mutation rates were then multiplied by the total genome length excluding repeat regions (3,041,373,115 bp) and further doubled.

Analysis of mutational signatures

Mutational signature analysis of single base substitutions (SBSs) and small indels were carried out using the nonnegative least squares method. The mutational signature was represented by 96 patterns of SBSs and 83 patterns of small indels (Alexandrov et al. 2020). Prelearned catalogs of mutational signatures in COSMIC (Sondka et al. 2024) were used to fit individual samples with a known set of signatures for each tissue type. SBS2 and SBS13 (known APOBEC-associated signatures) were included for all cases.

Calling RNA editings

VarScan2 was utilized to identify RNA editing. WGS of first single-cell cloned lines served as the paired normal reference. RNA editings were filtered with in-house Python script with the pysam module (see Supplemental Methods). To compare the RNA editing counts across samples, the number of RNA editings was normalized by a total base count. The total base count was calculated using SAMtools, considering only reads with mapping and base quality >20. The lowest total base count (3.1 Gb) was used as the normalization baseline. After calculating the normalization factor, the adjusted total depth of variant position and variant read counts were filtered with the same criteria. Recurrent RNA editing sites were defined as those observed in at least one sample treated with 0.1 µg/mL or 3 µg/mL doxycycline with the normalized callset.

Analysis of RNA editing signatures

RNA editing signatures were obtained by a modified version of the mutational signature extraction method described in previous studies (Alexandrov et al. 2013; Youk et al. 2024). Briefly, nonnegative matrix factorization (NMF) was utilized to disentangle an individual RNA editing spectrum based on a notion of mixed spectra (see Supplemental Methods; Cichocki et al. 2006; Roux et al. 2015). A total of 18 samples (three samples each of 0 µg/mL, 0.1 µg/mL, and 3 µg/mL APOBEC3 exposure with hGO_{1A3A} and hGO_{1A3B}) were analyzed by splitting into two subsets: A3A and A3B sets.

Analysis of secondary structure of RNA editing sites

The secondary structures of RNA editing sites were predicted as described previously (Jalili et al. 2020). Briefly, a 41-bp sequence centered on each RNA editing site in the canonical mRNA was used to assess secondary structure potential. Stem strength was calculated as $3 \times G/C$ pair + $1 \times A/T$ pair in stem. Among candidate structures, the most probable one was selected based on the following hierarchical criteria: (1) highest stem strength; (2) greatest number of G/C pairs in the stem; and (3) smallest loop size.

Calling structural variations

Structural variations were identified using DELLY v0.7.6 (Rausch et al. 2012). Raw calls were filtered using in-house scripts from our previous reports (Lee et al. 2019). The final call set was manually reviewed by the Integrative Genomics Viewer (Robinson et al. 2011).

DNA deaminase activity assay

The cytosine deaminase activity assay against DNA was conducted based on the previous literature with slight modifications (Buisson et al. 2019; Sanchez and Buisson 2025). Briefly, a total volume of 50 µL was prepared, containing either 8 µL of normalized cell ly-

sates or recombinant APOBEC3A (1:8 dilution) from an NEBNext Enzymatic Methyl-seq kit (New England Biolabs, #E7120S), and 42 µL of reaction buffer. The reaction buffer consisted of 20 pmol DNA oligonucleotide, 50 mM Tris (pH 7.5), 1.5 U of uracil DNA glycosylase (New England Biolabs, #M2080S), RNase A (0.1 µg/mL; Thermo Fisher Scientific, #EN0531), and 10 mM EDTA. The DNA oligonucleotide was synthesized by Integrated DNA Technologies with the sequence: 5'-(6-FAM)GCAAGCTGTTCA GCTTGCTGA-3'.

The reaction mixture was incubated at 37°C for 40 min, followed by the addition of 0.5 µL of 10 N NaOH and further incubation at 95°C for 40 min. Then, 50 µL of formamide was added, and the mixture was incubated at 95°C for 10 min, followed by cooling at 4°C for 5 min. For analysis, 5 µL of each sample were mixed with an equal volume of Gel Loading Buffer II (Thermo Fisher Scientific, #AM8546G) and incubated at 95°C for 5 min. Separation of the DNA oligonucleotides was performed on a Novex TBE-Urea Gel, 15% (Invitrogen, #EC6885BOX) by electrophoresis at 150 V for 60 min. Imaging was performed using the ibright CL750 Imaging System (Invitrogen).

In vitro deamination of DNA with recombinant APOBEC3B

The NEBNext Enzymatic Methyl-seq (EM-seq) kit (NEB, #E7120S) was utilized, following the manufacturer's protocol, for DNA library construction with slight modifications. Ten picograms of input DNA were utilized for the library construction. For the deamination steps, recombinant APOBEC3B, synthesized by EUPROTEIN INC., was used. The deamination step with APOBEC enzymes were conducted for 30 and 60 sec. Library amplification steps followed the BotSeqS library construction.

Detection of cytosine deamination by recombinant APOBEC3B in vitro

The BotSeqS variant calling pipeline was utilized with slight modifications. Among the criteria, the distances from read ends were excluded. Initially, all filtered mutations were collected. Among mutations in grouped DNA, only those located in DNA fragments where only one strand was mapped were counted. To calculate the genome-wide mutation rates, the BotSeqS pipeline was utilized, with the exception that cytosines or guanines were counted in a strand-specific manner. Because original methylated CpG sites were preserved during the library construction, both total base counts and mutation counts in CpG contexts were excluded from the analysis. To calculate mutation rates in DNA fragments containing at least one C>T variant, the genomic ranges of such fragments were identified using BEDTools (Quinlan and Hall 2010), considering the strand orientation. After this step, cytosines or guanines outside of CpG contexts were counted.

Analysis of 4-bp context mutations

SNVs from 10 hGO_{1A3A} samples (excluding control samples) and six TP53KO-hGO_{1A3B} samples were utilized in the analysis. Among 567 PCAWG samples across eight cancer types with a high prevalence of APOBEC mutational activity—breast adenocarcinoma (BRCA; n = 195), esophageal adenocarcinoma (ESAD; n = 97), stomach adenocarcinoma (STAD; n = 68), head-and-neck squamous cell carcinoma (HNSC; n = 56), lung squamous cell carcinoma (LUSC; n = 47), uterine corpus endometrial carcinoma (UCEC; n = 44), lung adenocarcinoma (LUAD; n = 37), and bladder urothelial carcinoma (BLCA; n = 23)—only samples with a combined clonal APOBEC-associated mutational burden (SBS2+SBS13) greater than 5000 were selected for this analysis (n = 63). This subject included: LUSC (n = 15), BRCA (n = 12), BLCA (n = 11), HNSC

(n = 13), LUAD (n = 6), UCEC (n = 3), ESAD (n = 2), and STAD (n = 1). Only clonal mutations were utilized for the analysis.

Calling clustered mutations

SigProfilerClusters (Bergstrom et al. 2022a), a Python module, was utilized to identify clustered mutations. FlexMix, R package (Leisch 2004), was utilized to classify the identified clustered mutations into *omikli* and *kataegis*. Because the tool determines the intermutation distance threshold through simulations that randomly distribute SNVs, the total number of SNVs influences the detection rate of clustered mutation events. To correct for the number of clustered mutation events, simulations were conducted (see Supplemental Methods; Supplemental Fig. S16). The “drm” function in the drc, R package (Ritz et al. 2019), was utilized for the analysis. To compare clustered mutation events, 146 samples from the PCAWG database were selected based on the following criteria: (1) nine cancer types showing high prevalence of APOBEC mutational signatures; and (2) samples with fewer than 500 SBS2+SBS13 were excluded in both our samples and PCAWG cancer samples to avoid bias.

Analysis of mutation rates based on epigenetic marker

Relative risk of mutation rates between signal and nonsignal regions was analyzed for each epigenetic marker, based on previous studies (Supek and Lehner 2017; Nam et al. 2023). Genome-wide signals for each marker, including replication timing, were downloaded from Roadmap Epigenomics Consortium for eight cell types (E017, E114, E117, E118, E119, E122, E125, and E127). Fold-enrichment signals were averaged, and regions with values <1 were defined as bin0 (nonsignal); all others were classified as signal-detected. SNVs were counted in each region, and relative risks were calculated, accounting for 3-bp genomic context.

For APOBEC-associated mutations, cytosines in the TCN context were considered as background, and C>T and C>G substitutions at these sites were counted. For SBS5 and SBS40, all thymine bases except within TCN context were used as the reference, and T>A, T>G, T>C, C>T, and C>G substitutions were counted. C>A mutations were excluded to avoid overlapping signals with SBS1 and SBS18.

For replication timing and H3K27me3, signal-detected regions were further divided into four equal-length bins to assess fold-enrichment. For transcriptional activity, TPM values in each base were derived from RNA-seq of doxycycline-treated organoids (3 µg/mL, 48 h). Using the “hg19_refGene.txt” file from ANNOVAR (Wang et al. 2010), only genic regions were analyzed. Genes with TPM=0 were defined as bin0; TPM>0 regions were binned by quartiles (bin1=0.05, bin2=1.73, and bin3 and bin4=9.68). To account for interactions among transcription, H3K27me3, and replication timing, enrichment analysis was performed using the glm.nb() function from the MASS R package (Venables and Ripley 2003) as described in previous research (Supek and Lehner 2017).

Analysis of mutation rates based on genomic location

SNVs located in previously described mappable regions were utilized throughout the analysis. Gene annotations from the “hg19_refGene.txt” file were utilized to match the additional information of position of SNVs. Classification of subgenic regions (5’-/3’-UTR, protein coding sequence [CDS], and intron) and transcription strand orientation was also based on this gene information. All merged genic regions were used as reference for discrimination of genic and intergenic regions.

For subgenic mutation rate comparisons, only non-overlapping genic regions and CDS regions flanked by introns were used, following a previously reported approach (Frigola et al. 2017).

Comparison of single nucleotide variants (SNVs) between reference genome versions

SNVs were additionally identified using human GRCh38 genome sequence. Coordinates of SNVs based on GRCh37 were converted to GRCh38 using BCFtools/liftover for comparative analysis (Supplemental Fig. S14; Genovese et al. 2024).

Publicly available data sets

Publicly available whole-genome sequencing data were utilized to demonstrate copy number variation in the normal human gastric organoid. WGS of blood from HC05 sample was utilized as the unpaired normal sample (obtained from the European Genome-phenome Archive [EGA; <https://ega-archive.org>] under accession number EGAS00001006213) (Nam et al. 2023). To compare the 4-bp-context preference and frequency of clustered mutation, SNV calls from the ICGC/TCGA Pan-Cancer Analysis of Whole-Genome (PCAWG) Consortium were utilized for the analysis. The callset data are available for download at <https://docs.icgc-argo.org/docs/data-access/icgc-25k-data#relocated-icgc-25k-data>.

We analyzed publicly available Smart-seq-based single-cell RNA-seq data sets from five cancer types: (1) lung adenocarcinoma (obtained from the NCBI BioProject database [<https://www.ncbi.nlm.nih.gov/bioproject/>] under accession number PRJNA591860) (Maynard et al. 2020); (2) head-and-neck squamous cell carcinoma (BioProject: accession number PRJNA401654; Gene Expression Omnibus [GEO; <https://www.ncbi.nlm.nih.gov/geo/>]: GSE103322) (Puram et al. 2017); (3) triple negative breast cancer (BioProject: PRJNA485423; GEO: GSE118390) (Karaayvaz et al. 2018); and (4) esophageal adenocarcinoma and esophageal squamous cell carcinoma (BioProject: PRJNA401501) (Wu et al. 2018).

In addition, we analyzed publicly available whole transcriptomic sequencing data of SARS-CoV-2-infected human gastric organoid (BioProject: PRJNA643724; GEO: GSE153698) (Giobbe et al. 2021) for the correlation between viral infections and expression of APOBEC family genes in human gastric organoid.

Quantification and statistical analysis

All statistical analyses were performed with R version 4.1.3 (<https://www.npackd.org/p/r/4.1.3>). A two-tailed one-sample *t*-test was used to evaluate *P*-values for comparing APOBEC-associated SNVs and expression levels between the groups. Linear regressions were conducted using the basic “lm” function in R to analyze the association among APOBEC-associated SNVs, ID9, SBS5, and SBS40. A χ^2 test was utilized to evaluate *P*-values for comparing replication strand bias and transcription strand bias. A 95% confidence interval was used to determine the statistical range of continuous data.

Data access

All raw and processed sequencing data generated in this study have been submitted to the Korean Nucleotide Archive (KoNA; <https://kbds.re.kr/KRA>) under accession number KAP240815. Essential in-house scripts used in this study are available on Zenodo (<https://doi.org/10.5281/zenodo.12771074>) and as Supplemental Code.

Competing interest statement

Y.S.J. is a genomic cofounder of Inocras Inc. All other authors declare no competing interests.

Acknowledgments

The authors thank Youngwon Cho (Epithelial Biology Center, Vanderbilt University Medical Center) for help with the cell viability test, Myungsook Choi (KAIST) for technical help for organoids, and Mia Petljak (New York University) for her valuable advice and feedback on the manuscript. This work was supported by the Young Investigator Grants from the Human Frontier Science Program (RGY0071/2018 to Y.S.J., B.-K.K., and H.S.); the National Research Foundation of Korea (Leading Researcher Program NRF-2020R1A3B2078973 to Y.S.J.); the Korea Bio Data Station (N24NM016-24 to J.L. and J.W.P.); and the Institute for Basic Science (IBS-R021-D1 to B.-K.K.).

Author contributions: Y.S.J., B.-K.K., and H.S. designed the experiments. J.-H.K. provided human gastric epithelium samples from biopsy. Y.J.B. established organoids from primary human gastric tissues. J.L. and J.W.P. helped with basic bioinformatic works (alignment and calling somatic variants). J.-H.L. and J.Y. conducted vector cloning. Y.A. and T.K. conducted the transformation of organoids, with J.-H.L. and J.Y. providing advice. Y.A. performed organoid culture, clonal expansion, and DNA/RNA extraction. B.-K.K. and H.K. provided training in organoids culture technologies. Y.A. performed cell viability analysis. J.-H.L. performed immunohistochemistry. S.A.O. conducted in vitro deamination experiments and most of the library construction including WGS and RNA-seq. Y.A., J.-H.P., and K.Y. conducted library construction for duplex sequencing analysis. Y.A. conducted most bioinformatic analyses, including alignment, mutation calling, duplex sequencing analysis, and analysis of expression levels with bulk RNA-seq data, with S.P., J.Y., and Y.S.J. providing advice. Y.A. and Jo.L. conducted quantitative and statistical data analysis. Y.A. and Jo.L. conducted mutational signature analysis including RNA editing. W.H.L. helped with the construction of the pipeline for analysis of duplex sequencing. Y.A. and C.H.N. conducted epigenomic analysis of variants and comparing variants based on two reference genomes, GRCh37 and GRCh38. H.L., J.H., and T.M.K. conducted the western blotting experiment.

References

Abascal F, Harvey LMR, Mitchell E, Lawson ARJ, Lensing SV, Ellis P, Russell AJC, Alcantara RE, Baez-Ortega A, Wang Y, et al. 2021. Somatic mutation landscapes at single-molecule resolution. *Nature* **593**: 405–410. doi:10.1038/s41586-021-03477-4

Alexandrov LB, Nik-Zainal S, Wedge DC, Campbell PJ, Stratton MR. 2013. Deciphering signatures of mutational processes operative in human cancer. *Cell Rep* **3**: 246–259. doi:10.1016/j.celrep.2012.12.008

Alexandrov LB, Kim J, Haradhvala NJ, Huang MN, Tian Ng AW, Wu Y, Boot A, Covington KR, Gordenin DA, Bergstrom EN, et al. 2020. The repertoire of mutational signatures in human cancer. *Nature* **578**: 94–101. doi:10.1038/s41586-020-1943-3

Alonso de la Vega A, Temiz NA, Tasakis R, Somogyi K, Salgueiro L, Zimmer E, Ramos M, Diaz-Jimenez A, Chocarro S, Fernández-Vaquero M, et al. 2023. Acute expression of human APOBEC3B in mice results in RNA editing and lethality. *Genome Biol* **24**: 267. doi:10.1186/s13059-023-03115-4

Amador V, Ge S, Santamaría PG, Guardavaccaro D, Pagano M. 2007. APC/c (Cdc20) controls the ubiquitin-mediated degradation of p21 in prometaphase. *Mol Cell* **27**: 462–473. doi:10.1016/j.molcel.2007.06.013

Amouroux R, Campalans A, Epe B, Radicella JP. 2010. Oxidative stress triggers the preferential assembly of base excision repair complexes on open chromatin regions. *Nucleic Acids Res* **38**: 2878–2890. doi:10.1093/nar/gkp1247

Bartfeld S, Bayram T, van de Wetering M, Huch M, Begthel H, Kujala P, Vries R, Peters PJ, Clevers H. 2015. In vitro expansion of human gastric epithelial stem cells and their responses to bacterial infection. *Gastroenterology* **148**: 126–136.e6. doi:10.1053/j.gastro.2014.09.042

Bergstrom EN, Kundu M, Tbeileh N, Alexandrov LB. 2022a. Examining clustered somatic mutations with SigProfilerClusters. *Bioinformatics* **38**: 3470–3473. doi:10.1093/bioinformatics/btac335

Bergstrom EN, Luebeck J, Petljak M, Khandekar A, Barnes M, Zhang T, Steele CD, Pillay N, Landi MT, Bafna V, et al. 2022b. Mapping clustered mutations in cancer reveals APOBEC3 mutagenesis of ecDNA. *Nature* **602**: 510–517. doi:10.1038/s41586-022-04398-6

Buisson R, Langenbucher A, Bowen D, Kwan EE, Benes CH, Zou L, Lawrence MS. 2019. Passenger hotspot mutations in cancer driven by APOBEC3A and mesoscale genomic features. *Science* **364**: eaaw2872. doi:10.1126/science.aaw2872

Burns MB, Lackey L, Carpenter MA, Rathore A, Land AM, Leonard B, Refsland EW, Kotandeniya D, Tretyakova N, Nikas JB, et al. 2013. APOBEC3B is an enzymatic source of mutation in breast cancer. *Nature* **494**: 366–370. doi:10.1038/nature11881

Carpenter MA, Temiz NA, Ibrahim MA, Jarvis MC, Brown MR, Argyris PP, Brown WL, Starrett GJ, Yee D, Harris RS. 2023. Mutational impact of APOBEC3A and APOBEC3B in a human cell line and comparisons to breast cancer. *PLoS Genet* **19**: e1011043. doi:10.1371/journal.pgen.1011043

Cazzalini O, Scovassi AI, Savio M, Stivala LA, Proserpi E. 2010. Multiple roles of the cell cycle inhibitor p21^{CDKN1A} in the DNA damage response. *Mutat Res* **704**: 12–20. doi:10.1016/j.mrrrev.2010.01.009

Chan K, Roberts SA, Klimczak LJ, Sterling JF, Saini N, Malc EP, Kim J, Kwiatkowski DJ, Fargo DC, Mieczkowski PA, et al. 2015. An APOBEC3A hypermutation signature is distinguishable from the signature of background mutagenesis by APOBEC3B in human cancers. *Nat Genet* **47**: 1067–1072. doi:10.1038/ng.3378

Choi J-H, Pfeifer GP. 2005. The role of DNA polymerase eta in UV mutational spectra. *DNA Repair (Amst)* **4**: 211–220. doi:10.1016/j.dnarep.2004.09.006

Cichocki A, Zdunek R, Amari S. 2006. New algorithms for non-negative matrix factorization in applications to blind source separation. In *2006 IEEE International Conference on Acoustics Speech and Signal Processing Proceedings*, Toulouse, France, pp. V–V. doi:10.1109/ICASSP.2006.1661352

Dananberg A, Striepen J, Rozowsky JS, Petljak M. 2024. APOBEC mutagenesis in cancer development and susceptibility. *Cancers (Basel)* **16**: 374. doi:10.3390/cancers16020374

Delbos F, De Smet A, Faili A, Aoufouchi S, Weill J-C, Reynaud C-A. 2005. Contribution of DNA polymerase eta to immunoglobulin gene hypermutation in the mouse. *J Exp Med* **201**: 1191–1196. doi:10.1084/jem.20050292

DeWeerd RA, Németh E, Póti Á, Petryk N, Chen C-L, Hyrien O, Szűts D, Green AM. 2022. Prospectively defined patterns of APOBEC3A mutagenesis are prevalent in human cancers. *Cell Rep* **38**: 110555. doi:10.1016/j.celrep.2022.110555

Dobin A, Davis CA, Schlesinger F, Drenkow J, Zaleski C, Jha S, Batut P, Chaisson M, Gingeras TR. 2013. STAR: ultrafast universal RNA-seq aligner. *Bioinformatics* **29**: 15–21. doi:10.1093/bioinformatics/bts635

Durfee C, Temiz NA, Levin-Klein R, Argyris PP, Alsøe L, Carracedo S, Alonso de la Vega A, Proehl J, Holzhauer AM, Seeman ZJ, et al. 2023. Human APOBEC3B promotes tumor development in vivo including signature mutations and metastases. *Cell Rep Med* **4**: 101211. doi:10.1016/j.xcrm.2023.101211

Favero F, Joshi T, Marquard AM, Birkbak NJ, Krzystanek M, Li Q, Szallasi Z, Eklund AC. 2015. Sequenza: allele-specific copy number and mutation profiles from tumor sequencing data. *Ann Oncol* **26**: 64–70. doi:10.1093/annonc/mdu479

Fixman B, Díaz-Gay M, Qiu C, Margaryan T, Lee B, Chen XS. 2024. Validation of the APOBEC3A-mediated RNA single base substitution signature and proposal of novel APOBEC1, APOBEC3B, and APOBEC3G RNA signatures. *J Mol Biol* **436**: 168854. doi:10.1016/j.jmb.2024.168854

Frigola J, Sabarinathan R, Mularoni L, Muiños F, Gonzalez-Perez A, López-Bigas N. 2017. Reduced mutation rate in exons due to differential mismatch repair. *Nat Genet* **49**: 1684–1692. doi:10.1038/ng.3991

Fujii M, Matano M, Nanki K, Sato T. 2015. Efficient genetic engineering of human intestinal organoids using electroporation. *Nat Protoc* **10**: 1474–1485. doi:10.1038/nprot.2015.088

Gaebler A-M, Hennig A, Buczolic H, Weitz J, Welsch T, Stange DE, Pape K. 2020. Universal and efficient electroporation protocol for genetic engineering of gastrointestinal organoids. *J Vis Exp* **156**: 60704. doi:10.3791/60704

Genovese G, Rockweiler NB, Gorman BR, Bigdeli TB, Pato MT, Pato CN, Ichihara K, McCarroll SA. 2024. BCFtools/liftover: an accurate and

- comprehensive tool to convert genetic variants across genome assemblies. *Bioinformatics* **40**: btae038. doi:10.1093/bioinformatics/btae038
- Giobbe GG, Bonfante F, Jones BC, Gagliano O, Luni C, Zambaiti E, Perin S, Laterza C, Busslinger G, Stuart H, et al. 2021. SARS-CoV-2 infection and replication in human gastric organoids. *Nat Commun* **12**: 6610. doi:10.1038/s41467-021-26762-2
- Gnatt AL, Cramer P, Fu J, Bushnell DA, Kornberg RD. 2001. Structural basis of transcription: an RNA polymerase II elongation complex at 3.3 Å resolution. *Science* **292**: 1876–1882. doi:10.1126/science.1059495
- Green AM, Landry S, Budagyan K, Avgousti DC, Shalhout S, Bhagwat AS, Weitzman MD. 2016. APOBEC3A damages the cellular genome during DNA replication. *Cell Cycle* **15**: 998–1008. doi:10.1080/15384101.2016.1152426
- Hoang ML, Kinde I, Tomasetti C, McMahon KW, Rosenquist TA, Grollman AP, Kinzler KW, Vogelstein B, Papadopoulos N. 2016. Genome-wide quantification of rare somatic mutations in normal human tissues using massively parallel sequencing. *Proc Natl Acad Sci* **113**: 9846–9851. doi:10.1073/pnas.1607794113
- Hoopes JJ, Cortez LM, Mertz TM, Malc EP, Mieczkowski PA, Roberts SA. 2016. APOBEC3A and APOBEC3B preferentially deaminate the lagging strand template during DNA replication. *Cell Rep* **14**: 1273–1282. doi:10.1016/j.celrep.2016.01.021
- The ICGC/TCGA Pan-Cancer Analysis of Whole Genomes Consortium. 2020. Pan-cancer analysis of whole genomes. *Nature* **578**: 82–93. doi:10.1038/s41586-020-1969-6
- Jager M, Blokzijl F, Kuijk E, Bertl J, Vougioukalaki M, Janssen R, Besseling N, Boymans S, de Ligt J, Pedersen JS, et al. 2019. Deficiency of nucleotide excision repair is associated with mutational signature observed in cancer. *Genome Res* **29**: 1067–1077. doi:10.1101/gr.246223.118
- Jalili P, Bowen D, Langenbucher A, Park S, Aguirre K, Corcoran RB, Fleischman AG, Lawrence MS, Zou L, Buisson R. 2020. Quantification of ongoing APOBEC3A activity in tumor cells by monitoring RNA editing at hotspots. *Nat Commun* **11**: 2971. doi:10.1038/s41467-020-16802-8
- Karaayvaz M, Cristea S, Gillespie SM, Patel AP, Mylvaganam R, Luo CC, Specht MC, Bernstein BE, Michor F, Ellisen LW. 2018. Unravelling subclonal heterogeneity and aggressive disease states in TNBC through single-cell RNA-seq. *Nat Commun* **9**: 3588. doi:10.1038/s41467-018-06052-0
- Kazanov MD, Roberts SA, Polak P, Stamatoyannopoulos J, Klimczak LJ, Gordenin DA, Sunyaev SR. 2015. APOBEC-induced cancer mutations are uniquely enriched in early-replicating, gene-dense, and active chromatin regions. *Cell Rep* **13**: 1103–1109. doi:10.1016/j.celrep.2015.09.077
- Kim J, Mouw KW, Polak P, Braunstein LZ, Kamburov A, Kwiatkowski DJ, Rosenberg JE, Van Allen EM, D'Andrea A, Getz G. 2016. Somatic ERCC2 mutations are associated with a distinct genomic signature in urothelial tumors. *Nat Genet* **48**: 600–606. doi:10.1038/ng.3557
- Kim S, Scheffler K, Halpern AL, Bekritsky MA, Noh E, Källberg M, Chen X, Kim Y, Beyter D, Krusche P, et al. 2018. Strelka2: fast and accurate calling of germline and somatic variants. *Nat Methods* **15**: 591–594. doi:10.1038/s41592-018-0051-x
- Kim K, Shi AB, Kelley K, Chen XS. 2023. Unraveling the enzyme-substrate properties for APOBEC3A-mediated RNA editing. *J Mol Biol* **435**: 168198. doi:10.1016/j.jmb.2023.168198
- Koboldt DC, Zhang Q, Larson DE, Shen D, McLellan MD, Lin L, Miller CA, Mardis ER, Ding L, Wilson RK. 2012. VarScan 2: somatic mutation and copy number alteration discovery in cancer by exome sequencing. *Genome Res* **22**: 568–576. doi:10.1101/gr.129684.111
- Law EK, Levin-Klein R, Jarvis MC, Kim H, Argyris PP, Carpenter MA, Starrett GJ, Temiz NA, Larson LK, Durfee C, et al. 2020. APOBEC3A catalyzes mutation and drives carcinogenesis in vivo. *J Exp Med* **217**: e20200261. doi:10.1084/jem.20200261
- Lawrence MS, Stojanov P, Polak P, Kryukov GV, Cibulskis K, Sivachenko A, Carter SL, Stewart C, Mermel CH, Roberts SA, et al. 2013. Mutational heterogeneity in cancer and the search for new cancer-associated genes. *Nature* **499**: 214–218. doi:10.1038/nature12213
- Lawson ARJ, Abascal F, Coorens THH, Hooks Y, O'Neill L, Latimer C, Raine K, Sanders MA, Warren AY, Mahubani KTA, et al. 2020. Extensive heterogeneity in somatic mutation and selection in the human bladder. *Science* **370**: 75–82. doi:10.1126/science.aba8347
- Lee JJ-K, Park S, Park H, Kim S, Lee J, Lee J, Youk J, Yi K, An Y, Park IK, et al. 2019. Tracing oncogene rearrangements in the mutational history of lung adenocarcinoma. *Cell* **177**: 1842–1857.e21. doi:10.1016/j.cell.2019.05.013
- Lee J-H, Kim S, Han S, Min J, Caldwell B, Bamford A-D, Rocha ASB, Park J, Lee S, Wu S-HS, et al. 2022. p57^{Kip2} imposes the reserve stem cell state of gastric chief cells. *Cell Stem Cell* **29**: 826–839.e9. doi:10.1016/j.stem.2022.04.001
- Leisch F. 2004. FlexMix: a general framework for finite mixture models and latent class regression in R. *J Stat Softw* **11**: 1–18. doi:10.18637/jss.v011.i08
- Li H, Durbin R. 2010. Fast and accurate long-read alignment with Burrows–Wheeler transform. *Bioinformatics* **26**: 589–595. doi:10.1093/bioinformatics/btp698
- Li B, Dewey CN. 2011. RSEM: accurate transcript quantification from RNA-seq data with or without a reference genome. *BMC Bioinformatics* **12**: 323. doi:10.1186/1471-2105-12-323
- Li H, Handsaker B, Wysoker A, Fennell T, Ruan J, Homer N, Marth G, Abecasis G, Durbin R, 1000 Genome Project Data Processing Subgroup. 2009. The Sequence Alignment/Map format and SAMtools. *Bioinformatics* **25**: 2078–2079. doi:10.1093/bioinformatics/btp352
- Love MI, Huber W, Anders S. 2014. Moderated estimation of fold change and dispersion for RNA-seq data with DESeq2. *Genome Biol* **15**: 550. doi:10.1186/s13059-014-0550-8
- Maciejowski J, Chatziplis A, Dananberg A, Chu K, Toufektchan E, Klimczak LJ, Gordenin DA, Campbell PJ, de Lange T. 2020. APOBEC3-dependent kataegis and TREX1-driven chromothripsis during telomere crisis. *Nat Genet* **52**: 884–890. doi:10.1038/s41588-020-0667-5
- Martin M. 2011. Cutadapt removes adapter sequences from high-throughput sequencing reads. *EMBnetjournal* **17**: 10–12. doi:10.14806/ej.17.1.200
- Martínez-Ruiz C, Black JRM, Puttick C, Hill MS, Demeulemeester J, Larose Cadieux E, Thol K, Jones TP, Veeriah S, Naceur-Lombardelli C, et al. 2023. Genomic-transcriptomic evolution in lung cancer and metastasis. *Nature* **616**: 543–552. doi:10.1038/s41586-023-05706-4
- Matsushima K, Yang D, Oppenheim JJ. 2022. Interleukin-8: an evolving chemokine. *Cytokine* **153**: 155828. doi:10.1016/j.cyt.2022.155828
- Maynard A, McCoach CE, Rotow JK, Harris L, Haderk F, Kerr DL, Yu EA, Schenk EL, Tan W, Zee A, et al. 2020. Therapy-induced evolution of human lung cancer revealed by single-cell RNA sequencing. *Cell* **182**: 1232–1251.e22. doi:10.1016/j.cell.2020.07.017
- McKenna A, Hanna M, Banks E, Sivachenko A, Cibulskis K, Kernysky A, Garimella K, Altshuler D, Gabriel S, Daly M, et al. 2010. The Genome Analysis Toolkit: a MapReduce framework for analyzing next-generation DNA sequencing data. *Genome Res* **20**: 1297–1303. doi:10.1101/gr.107524.110
- Mihara E, Hirai H, Yamamoto H, Tamura-Kawakami K, Matano M, Kikuchi A, Sato T, Takagi J. 2016. Active and water-soluble form of lipidated Wnt protein is maintained by a serum glycoprotein afamin/α-albumin. *eLife* **5**: e11621. doi:10.7554/eLife.11621
- Nam CH, Youk J, Kim JY, Lim J, Park JW, Oh SA, Lee HJ, Park JW, Won H, Lee Y, et al. 2023. Widespread somatic L1 retrotransposition in normal colorectal epithelium. *Nature* **617**: 540–547. doi:10.1038/s41586-023-06046-z
- Naumann JA, Argyris PP, Carpenter MA, Gupta HB, Chen Y, Temiz NA, Zhou Y, Durfee C, Proehl J, Koniar BL, et al. 2023. DNA deamination is required for human APOBEC3A-driven hepatocellular carcinoma in vivo. *Int J Mol Sci* **24**: 9305. doi:10.3390/ijms2419305
- Nik-Zainal S, Alexandrov LB, Wedge DC, Van Loo P, Greenman CD, Raine K, Jones D, Hinton J, Marshall J, Stebbings LA, et al. 2012a. Mutational processes molding the genomes of 21 breast cancers. *Cell* **149**: 979–993. doi:10.1016/j.cell.2012.04.024
- Nik-Zainal S, Van Loo P, Wedge DC, Alexandrov LB, Greenman CD, Lau KW, Raine K, Jones D, Marshall J, Ramakrishna M, et al. 2012b. The life history of 21 breast cancers. *Cell* **149**: 994–1007. doi:10.1016/j.cell.2012.04.023
- Nordentoft I, Lamy P, Birkenkamp-Demtröder K, Shumansky K, Vang S, Hornshøj H, Juul M, Villesen P, Hedegaard J, Roth A, et al. 2014. Mutational context and diverse clonal development in early and late bladder cancer. *Cell Rep* **7**: 1649–1663. doi:10.1016/j.celrep.2014.04.038
- Okazaki R, Okazaki T, Sakabe K, Sugimoto K, Sugino A. 1968. Mechanism of DNA chain growth. I. Possible discontinuity and unusual secondary structure of newly synthesized chains. *Proc Natl Acad Sci* **59**: 598–605. doi:10.1073/pnas.59.2.598
- Otlu B, Díaz-Gay M, Vermes I, Bergstrom EN, Zhivagui M, Barnes M, Alexandrov LB. 2023. Topography of mutational signatures in human cancer. *Cell Rep* **42**: 112930. doi:10.1016/j.celrep.2023.112930
- Park S, Mali NM, Kim R, Choi J-W, Lee J, Lim J, Park JM, Park JW, Kim D, Kim T, et al. 2021. Clonal dynamics in early human embryogenesis inferred from somatic mutation. *Nature* **597**: 393–397. doi:10.1038/s41586-021-03786-8
- Petljak M, Alexandrov LB, Brummel J, Price S, Wedge DC, Grossmann S, Dawson KJ, Ju YS, Iorio F, Tubio JM, et al. 2019. Characterizing mutational signatures in human cancer cell lines reveals episodic APOBEC mutagenesis. *Cell* **176**: 1282–1294.e20. doi:10.1016/j.cell.2019.02.012
- Petljak M, Dananberg A, Chu K, Bergstrom EN, Striepen J, von Morgen P, Chen Y, Shah H, Sale JE, Alexandrov LB, et al. 2022. Mechanisms of

- APOBEC3 mutagenesis in human cancer cells. *Nature* **607**: 799–807. doi:10.1038/s41586-022-04972-y
- Pleguezuelos-Manzano C, Puschhof J, Rosendahl Huber A, van Hoeck A, Wood HM, Nomburg J, Gurjao C, Manders F, Dalmaso G, Stege PB, et al. 2020. Mutational signature in colorectal cancer caused by genotoxic *pks⁺ E. coli*. *Nature* **580**: 269–273. doi:10.1038/s41586-020-2080-8
- Puram SV, Tirosh I, Parkh AS, Patel AP, Yizhak K, Gillespie S, Rodman C, Luo CL, Mroz EA, Emerick KS, et al. 2017. Single-cell transcriptomic analysis of primary and metastatic tumor ecosystems in head and neck cancer. *Cell* **171**: 1611–1624.e24. doi:10.1016/j.cell.2017.10.044
- Quinlan AR, Hall IM. 2010. BEDTools: a flexible suite of utilities for comparing genomic features. *Bioinformatics* **26**: 841–842. doi:10.1093/bioinformatics/btq033
- Rausch T, Zichner T, Schlattl A, Stütz AM, Benes V, Korbel JO. 2012. DELLY: structural variant discovery by integrated paired-end and split-read analysis. *Bioinformatics* **28**: i333–i339. doi:10.1093/bioinformatics/bts378
- Rhind N, Gilbert DM. 2013. DNA replication timing. *Cold Spring Harb Perspect Biol* **5**: a010132. doi:10.1101/cshperspect.a010132
- Ritz C, Jensen SM, Gerhard D, Streibig JC. 2019. Dose-response analysis using R. *PLoS One* **10**: e0146021. doi:10.1371/journal.pone.0146021
- Roberts SA, Lawrence MS, Klimczak LJ, Grimm SA, Fargo D, Stojanov P, Kiezun A, Kryukov GV, Carter SL, Saksena G, et al. 2013. An APOBEC cytidine deaminase mutagenesis pattern is widespread in human cancers. *Nat Genet* **45**: 970–976. doi:10.1038/ng.2702
- Robinson JT, Thorvaldsdóttir H, Winckler W, Guttman M, Lander ES, Getz G, Mesirov JP. 2011. Integrative Genomics Viewer. *Nat Biotechnol* **29**: 24–26. doi:10.1038/nbt.1754
- Roux LJ, Weninger FJ, Hershey JR. 2015. Sparse NMF – half-baked or well done? Tech. Rep. No. TR2015-023. <https://www.merl.com/publications/docs/TR2015-023.pdf>.
- Saini N, Roberts SA, Sterling JF, Malc EP, Mieczkowski PA, Gordenin DA. 2017. APOBEC3B cytidine deaminase targets the non-transcribed strand of tRNA genes in yeast. *DNA Repair (Amst)* **53**: 4–14. doi:10.1016/j.dnarep.2017.03.003
- Sanchez A, Buisson R. 2025. An in vitro cytidine deaminase assay to monitor APOBEC activity on DNA. *Methods Enzymol* **713**: 201–219. doi:10.1016/bs.mie.2024.11.037
- Sanchez A, Ortega P, Sakhtemani R, Manjunath L, Oh S, Bourinque E, Becker A, Kim K, Durfee C, Temiz NA, et al. 2024. Mesoscale DNA features impact APOBEC3A and APOBEC3B deaminase activity and shape tumor mutational landscapes. *Nat Commun* **15**: 2370. doi:10.1038/s41467-024-45909-5
- Satija R, Farrell JA, Gennert D, Schier AF, Regev A. 2015. Spatial reconstruction of single-cell gene expression data. *Nat Biotechnol* **33**: 495–502. doi:10.1038/nbt.3192
- Sondka Z, Dhir NB, Carvalho-Silva D, Jupe S, Madhumita, McLaren K, Starkey M, Ward S, Wilding J, Ahmed M, et al. 2024. COSMIC: a curated database of somatic variants and clinical data for cancer. *Nucleic Acids Res* **52**: D1210–D1217. doi:10.1093/nar/gkad986
- Supek F, Lehner B. 2017. Clustered mutation signatures reveal that error-prone DNA repair targets mutations to active genes. *Cell* **170**: 534–547.e23. doi:10.1016/j.cell.2017.07.003
- van Ineveld RL, Ariese HCR, Wehrens EJ, Dekkers JF, Rios AC. 2020. Single-cell resolution three-dimensional imaging of intact organoids. *J Vis Exp* **160**: e60709. doi:10.3791/60709
- Venables WN, Ripley BD. 2003. *Modern applied statistics with S*. Springer Science & Business Media, Berlin/Heidelberg.
- Vieira VC, Soares MA. 2013. The role of cytidine deaminases on innate immune responses against human viral infections. *Biomed Res Int* **2013**: 683095. doi:10.1155/2013/683095
- Wang K, Li M, Hakonarson H. 2010. ANNOVAR: functional annotation of genetic variants from high-throughput sequencing data. *Nucleic Acids Res* **38**: e164. doi:10.1093/nar/gkq603
- Wang Y, Robinson PS, Coorens THH, Moore L, Lee-Six H, Noorani A, Sanders MA, Jung H, Katainen R, Heuschkel R, et al. 2023. APOBEC mutagenesis is a common process in normal human small intestine. *Nat Genet* **55**: 246–254. doi:10.1038/s41588-022-01296-5
- Wilson MH, Coates CJ, George AL Jr. 2007. *PiggyBac* transposon-mediated gene transfer in human cells. *Mol Ther* **15**: 139–145. doi:10.1038/sj.mt.6300028
- Woodard LE, Wilson MH. 2015. *piggyBac*-ing models and new therapeutic strategies. *Trends Biotechnol* **33**: 525–533. doi:10.1016/j.tibtech.2015.06.009
- Wu Y-Y, Tsai H-F, Lin W-C, Hsu P-I, Shun C-T, Wu M-S, Hsu P-N. 2007. Upregulation of CCL20 and recruitment of CCR6⁺ gastric infiltrating lymphocytes in *Helicobacter pylori* gastritis. *Infect Immun* **75**: 4357–4363. doi:10.1128/IAI.01660-06
- Wu H, Yu J, Li Y, Hou Q, Zhou R, Zhang N, Jing Z, Jiang M, Li Z, Hua Y, et al. 2018. Single-cell RNA sequencing reveals diverse intratumoral heterogeneities and gene signatures of two types of esophageal cancers. *Cancer Lett* **438**: 133–143. doi:10.1016/j.canlet.2018.09.017
- Wu T, Lyu R, You Q, He C. 2020. Kethoxal-assisted single-stranded DNA sequencing captures global transcription dynamics and enhancer activity in situ. *Nat Methods* **17**: 515–523. doi:10.1038/s41592-020-0797-9
- Yoshida K, Gowers KHC, Lee-Six H, Chandrasekharan DP, Coorens T, Maughan EF, Beal K, Menzies A, Millar FR, Anderson E, et al. 2020. Tobacco smoking and somatic mutations in human bronchial epithelium. *Nature* **578**: 266–272. doi:10.1038/s41586-020-1961-1
- Youk J, Kwon HW, Kim R, Ju YS. 2021. Dissecting single-cell genomes through the clonal organoid technique. *Exp Mol Med* **53**: 1503–1511. doi:10.1038/s12276-021-00680-1
- Youk J, Kwon HW, Lim J, Kim E, Kim T, Kim R, Park S, Yi K, Nam CH, Jeon S, et al. 2024. Quantitative and qualitative mutational impact of ionizing radiation on normal cells. *Cell Genom* **4**: 100499. doi:10.1016/j.xgen.2024.100499

Received December 12, 2024; accepted in revised form August 22, 2025.



APOBEC3A drives deaminase mutagenesis in human gastric epithelium

Yohan An, Ji-Hyun Lee, Joonoh Lim, et al.

Genome Res. 2025 35: 2158-2172 originally published online August 26, 2025

Access the most recent version at doi:[10.1101/gr.280338.124](https://doi.org/10.1101/gr.280338.124)

Supplemental Material <http://genome.cshlp.org/content/suppl/2025/09/12/gr.280338.124.DC1>

References This article cites 94 articles, 11 of which can be accessed free at:
<http://genome.cshlp.org/content/35/10/2158.full.html#ref-list-1>

Open Access Freely available online through the *Genome Research* Open Access option.

Creative Commons License This article, published in *Genome Research*, is available under a Creative Commons License (Attribution-NonCommercial 4.0 International), as described at <http://creativecommons.org/licenses/by-nc/4.0/>.

Email Alerting Service Receive free email alerts when new articles cite this article - sign up in the box at the top right corner of the article or [click here](#).



To subscribe to *Genome Research* go to:
<https://genome.cshlp.org/subscriptions>
